INTERNATIONAL JOURNAL FOR NUMERICAL METHODS IN FLUIDS
Int. J. Numer. Meth. Fluids 2009; **61**:606–637
Published online 2 December 2008 in Wiley InterScience (www.interscience.wiley.com). DOI: 10.1002/fld.1968

Instabilities of Boussinesq models in non-uniform depth

F. Løvholt[1,*,†] and G. Pedersen[2]

[1]*Norwegian Geotechnical Institute, Computational Geomechanics Division, P.O. Box 3930, Ullevål Stadion, N0806 Oslo, Norway*
[2]*Department of Mathematics, University of Oslo, Box 1053 Blindern, N-0316, Norway*

SUMMARY

The von Neumann method for stability analysis of linear waves in a uniform medium is a widely applied procedure. However, the method does not apply to stability of linear waves in a variable medium. Herein we describe instabilities due to variable depth for different Boussinesq equations, including the standard model by Peregrine and the popular generalization by Nwogu. Eigenmodes are first found for bathymetric features on the grid scale. For certain combinations of Boussinesq formulations and bottom profiles stability limits are found in closed form, otherwise numerical techniques are used for the eigenvalue problems. Naturally, the unstable modes in such settings must be considered to be as much a result of the difference method as of the underlying differential (Boussinesq) equations. Hence, modes are also computed for smooth depth profiles that are well resolved. Generally, the instabilities do not vanish with refined resolution. In some cases convergence is observed and we thus have indications of unstable solutions of the differential equations themselves. The stability properties differ strongly. While the standard Boussinesq equations seem perfectly stable, all the other formulations do display unstable modes. In most cases the instabilities are linked to steep bottom gradients and small grid increments. However, while a certain formulation, based on velocity potentials, is very prone to instability, the Boussinesq equations of Nwogu become unstable only under quite demanding conditions. Still, for the formulation of Nwogu, instabilities are probably inherent in the differential equations and are not a result of the numerical model. Copyright © 2008 John Wiley & Sons, Ltd.

Received 25 June 2007; Revised 17 September 2008; Accepted 10 October 2008

KEY WORDS: tsunamis; surface waves; stability and convergence of numerical models; eigenvalue analysis; Boussinesq equations; linear dispersive waves

*Correspondence to: F. Løvholt, Norwegian Geotechnical Institute, Computational Geomechanics Division, P.O. Box 3930, Ullevål Stadion, N-0806 Oslo, Norway.
†E-mail: flo@ngi.no

Contract/grant sponsor: The Research Council of Norway; contract/grant number: 154831
Contract/grant sponsor: International Centre for Geohazards
Contract/grant sponsor: Norwegian Geotechnical Institute

1. INTRODUCTION

The traditional dispersive long wave formulations, namely the Boussinesq and KdV equations, go back to the 19th century and have been important tools for the evolution of theoretical concepts of wave theory. Important examples are the breakthroughs in soliton interaction and inverse scattering theory in 1960–1980. With the availability of computers the Boussinesq equations found new applications through numerical solutions. Pioneering works are studies of undular bores [1] and shoaling of solitary waves [2], while a large number of numerical studies based on Boussinesq-type equations have been published to this day.

In the last decades we have seen considerable development on long wave expansions. New Boussinesq-type formulations, such as those introduced by Madsen *et al*. [3] and Nwogu [4], displayed improved accuracy, as well as extended validity ranges in comparison with the standard versions. Progress was made with respect to both dispersion properties, that are relevant for the present study, and non-linearities that are much less so. A variety of forms for numerical modeling [5–13] were then proposed, but markedly smaller samples have been put to work in existing models. In parallel, Boussinesq-type models have been applied to increasingly demanding problems in coastal engineering and the performance of such equations on constant, or mildly varying depth, has been extensively investigated. On the other hand, the effects of rapid bottom variations, which frequently appear in real simulations, are hardly studied in a general context [14]. Our experience, which also motivates the present work, is that effects of this kind, in the form of instabilities, indeed may occur. As we will demonstrate subsequently the instabilities may be owing both to the partial differential equations (PDEs) and the numerical solution procedures.

The standard tool for stability analysis is the von Neumann method where linear wave propagation in uniform media and grids is studied. Generally, the results are simple stability criteria of the CFL type, with the frequent interpretation that the discrete signal speed should not be smaller than the physical wave speed. Such criteria are then often, and in many circumstances successfully, conveyed to more complex situations, where *ad hoc* modifications are made to CFL-type criteria to include variable coefficients. However, it is generally recognized that non-linearity may give rise to instabilities and spurious phenomena that are not contained in the von Neumann analysis [15]. Hence, even if most non-linear models evade rigorous analysis there is an awareness concerning their performance that urges for some measure of testing and careful investigation of results. On the other hand, spurious effects related to variable coefficients (depth or grid) have traditionally received little attention. Nevertheless, investigations that have been carried out indicate that such problems do exist. For instance, an eigenvalue analysis of the propagation matrices of one of the standard models for ocean waves revealed that the Coriolis effect, in combination with variable depth, may lead to instabilities in the form of exponentially growing modes [16].

In this paper we first present briefly (Section 2) one of several applications where peculiar instabilities ruined Boussinesq simulations. It was soon revealed that the instabilities were of a linear type and linked to steep bottom gradients that were resolved with a fine grid. To our knowledge, neither this type of phenomenon nor a systematic stability investigation of Boussinesq equations in variable depth have ever been published. We then identify the instability in the simplest possible context, namely that of linear, plane wave motion in simple bathymetries. These efforts are presented in Sections 5–6, preceded by Sections 3 and 4 that contain the necessary background on equations and numerical methods. Readers with little interest for mathematical and numerical details may skip Sections 3 and 4 and still be able to follow the main lines in the proceeding sections.

DOI: 10.1002/fld

Our investigation involves numerical solution of a selection of linearized Boussinesq formulations from the literature, in simplified geometries such as idealized sea mounts and shelves in finite and infinite basins. Instabilities are then sought as eigenoscillations with growing amplitudes. In a few cases we may find closed-form expressions for the eigenmodes and even rudimentary stability criteria. However, generally we must resort to numerical solution procedures for the eigenvalue problems. Indeed, we do find variable depth instabilities for all the investigated Boussinesq formulations, save one. However, the instabilities display a high degree of diversity concerning their nature, occurrence and severity. Therefore, they elude a common classification. Neither are we able to find a simple explanation; in some cases the instability seems to be crucially dependent on the numerical method while in other cases it is apparently rooted in PDEs themselves. Naturally, a general and comprehensible explanation may not exist for spurious phenomena such as these. Still, we are able to conclude that some formulations should be avoided due to the instabilities in question, whereas others are not likely to have them in realistic simulations.

2. AN EXAMPLE OF INSTABILITY IN A BOUSSINESQ-TYPE MODEL

Rockslides in Norwegian fjords have caused several destructive tsunamis in the last centuries [17]. The most recent of the larger events is the Tafjord tsunami in 1934, which previously has been analyzed with a linear hydrostatic model [18]. However, in view of bathymetry and wave periods the propagation of the Tafjord tsunami may have been dispersive. The complex geometry and need for flexible resolution then led us to attempt a finite element Boussinesq model [19]. In a preliminary investigation we replaced the slide by a mid-fjord initial condition, with an extent that roughly matches the wavelengths found by Harbitz *et al*. [18], and omit the non-linearity. Rapidly, huge surface elevations appeared at a location close to, but not at, the shoreline. The instability is illustrated in Figure 1. Whereas this instability spread only slightly and remained confined to a few nodes, similar artificial surface peaks subsequently appeared at other separate locations as well. Time series at the locations of instability (not shown) displayed exponential growth.

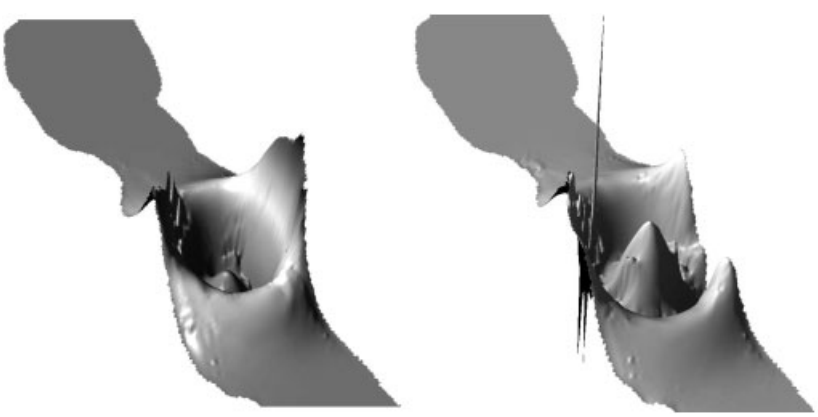

Figure 1. Simulation of the wave propagation in Tafjorden in the initial phase ($t = 12.5$ s) of the instability, (left panel). The instability at a later stage ($t = 15.7$ s) is shown in the right panel.

DOI: 10.1002/fld

A number of actions were taken to remove the instability. The most obvious option was to reduce the time step, but this did not decrease the growth rate of the instabilities significantly. Other attempts, like applications of adaptive grids, rectangular grids, and perturbing the nodes close to the initial point of the instability, changing the element type and order, and lumping the mass matrix to mimic a finite difference technique, were equally unfruitful. This suggested that the instability was not caused by the numerical discretization, but was inherent in the Boussinesq formulation itself. In fact, the authors proposing the method employed in question [19] did report irregularities that may be linked to the instability encountered in the Tafjord simulation. Moreover, we have detected similar instabilities in other applications, such as tsunamis interacting with sea mounts in the Atlantic Ocean. Hence, we were led to investigate the instability more formally in a simpler context, but for a broad range of Boussinesq formulations.

3. FORMULATION

We introduce a Cartesian coordinate system with horizontal axes, ox^* and oy^* in the undisturbed water level and an oz^* axis pointing vertically upward. Stars indicate quantities with dimension. In the formulation of the equations we employ a typical depth d and a typical wavelength L as vertical and horizontal length scales, respectively. Then, the time scale becomes $t_c = L/\sqrt{gd}$, where g is the acceleration of gravity. Introducing a dimensionless amplitude factor, ε, we define $\varepsilon L/t_c$, $\varepsilon d/t_c$ and εd as scales for horizontal velocity, vertical velocity and surface elevation, respectively. As we exclusively study the linearized equations, the choice of ε only concerns the presentation of the results. Hence, this parameter will generally be chosen so as to yield a scaled amplitude, for surface elevation, equal to unity.

3.1. Boussinesq-type equations

Consistent inclusion of second-order terms in μ yields Boussinesq-type equations that are available in many varieties [8, 20, 21]. We will group the equations into two main types, according to whether velocities or velocity potentials are used as primary unknowns. Confining ourselves to one dimension of propagation, linearized, we write generic Boussinesq equations based on velocities according to

$$\frac{\partial \eta}{\partial t} = -\frac{\partial Q}{\partial x} + O(\mu^4), \quad Q = hu + \mu^2 Q_1 \tag{1}$$

$$\frac{\partial u}{\partial t} = -\frac{\partial \eta}{\partial x} + \mu^2 D_u + O(\mu^4) \tag{2}$$

where η is the surface elevation, Q is the vertically integrated volume flux and u is the velocity, that may be evaluated at a given vertical position or as a depth integrated average. If we employ a velocity potential, ϕ, which again may be evaluated at a given vertical location or as an vertical average, as primary unknown we obtain

$$\frac{\partial \eta}{\partial t} = -\frac{\partial Q}{\partial x} + O(\mu^4), \quad Q = h\frac{\partial \phi}{\partial x} + \mu^2 Q_1 \tag{3}$$

$$\frac{\partial \phi}{\partial t} + \eta - \mu^2 D_\phi = O(\mu^4) \tag{4}$$

DOI: 10.1002/fld

This form inherits a few computational advantages over (1) and (2) concerning extension to wave propagation in two dimensions and the application of the finite element method. However, as will be demonstrated subsequently, some potential formulations are particularly prone to spurious behavior in variable depth.

Herein we study a selection of Boussinesq formulations including

- *The standard velocity formulation*, with the depth-averaged velocity as unknown, as first solved numerically in variable depth by Peregrine [2].
- *The generalized velocity formulation* proposed by Nwogu [4], which employs the velocities at vertical positions $z=z_\alpha(x,y)$ as unknowns. An optimal choice is $z_\alpha/h=-0.531$, while $z_\alpha/h=(1/\sqrt{3}-1)$ reproduces the standard formulation on constant depth. In variable depth, however, the two formulations may have very different properties.
- *The standard potential formulation* with the depth averaged velocity potential as unknown [19]. This is the formulation employed in the example in Section 2. In constant depth this formulation becomes equivalent to the standard formulation with depth averaged velocities, also in the discrete versions presented subsequently.
- *The mild-slope formulation*. Assuming a gently varying bathymetry a mild-slope version of the previous set may be obtained by deleting all depth gradients in $O(\mu^2)$ terms. In analogy to [22] an $O(\mu^4)$ correction term is added to the Bernoulli equation. Through variation of a free parameter, κ, the dispersion properties of the Nwogu formulations may be reproduced.
- *A generalized potential formulation* with the potential at the position z_α as unknown [6]. The role of the z_α is the same as for the equations of Nwogu.

The explicit forms of the dispersion terms are given in Table I. Throughout the paper, the abbreviation *improved* is used whenever $z_\alpha/h=-0.531$ is used in the generalized formulations.

Table I. The order μ^2 terms for the different Boussinesq formulations investigated herein. The primary unknown representing horizontal motion and a few references are given in the left column.

Standard velocity formulation	$Q_1=0$
Averaged velocity [2, 20]	$D_u=\frac{1}{2}h\frac{\partial^2}{\partial x^2}\left(h\frac{\partial u}{\partial t}\right)-\frac{1}{6}h^2\frac{\partial^3 u}{\partial x^2\partial t}$
Generalized velocity formulation	$Q_1=h(\frac{1}{2}z_\alpha^2-\frac{1}{6}h^2)\frac{\partial^2 u}{\partial x^2}+h(z_\alpha+\frac{1}{2}h)\frac{\partial^2(hu)}{\partial x^2}$
Velocity at $z=z_\alpha(x,y)$ [4]	$D_u=-z_\alpha\frac{\partial^2}{\partial x^2}\left(h\frac{\partial u}{\partial t}\right)-\frac{1}{2}z_\alpha^2\frac{\partial^3 u}{\partial x^2\partial t}$
Standard potential formulation	$Q_1=h\left(\frac{1}{6}\frac{\partial\eta}{\partial t}-\frac{1}{3}\frac{\partial h}{\partial x}\frac{\partial\phi}{\partial x}\right)\frac{\partial h}{\partial x}$
Averaged potential [21, 19]	$D_\phi=\frac{1}{2}h\frac{\partial}{\partial x}\left(h\frac{\partial^2\phi}{\partial x\partial t}\right)-\frac{1}{6}h^2\frac{\partial^3\phi}{\partial x^2\partial t}$
Mild-slope formulation	$Q_1=0$
Averaged potential	$D_\phi=h^2\left(\kappa\frac{\partial^2\eta}{\partial x^2}+\left(\frac{1}{3}+\kappa\right)\frac{\partial^3\phi}{\partial x^2\partial t}\right)$
Generalized potential formulation	$Q_1=h\frac{\partial}{\partial x}\left(z_\alpha\frac{\partial}{\partial x}\left(h\frac{\partial\phi}{\partial x}\right)+\frac{z_\alpha^2}{2}\frac{\partial^2\phi}{\partial x^2}\right)+\frac{h^2}{2}\frac{\partial^2}{\partial x^2}\left(h\frac{\partial\phi}{\partial x}\right)-\frac{h^3}{6}\frac{\partial^3\phi}{\partial x^3}$
Potential at $z=z_\alpha(x,y)$ [6]	$D_\phi=-\frac{1}{2}z_\alpha^2\frac{\partial^3\phi}{\partial x^2\partial t}-z_\alpha\frac{\partial}{\partial x}\left(h\frac{\partial^2\phi}{\partial x\partial t}\right)$

DOI: 10.1002/fld

3.2. Numerical techniques

We employ a simple formalism that will increase the readability of subsequent expressions. The approximation to a quantity f at a grid point with coordinates $(\beta\Delta x, \kappa\Delta t)$, where Δx and Δt are the grid increments, is denoted by $f_\beta^{(\kappa)}$. To make the difference equations more compact and legible we introduce the symmetric difference and average operators, δ_x and $-x$ by

$$\delta_x f_\beta^{(\kappa)} = \frac{1}{\Delta x}(f_{\beta+1/2}^{(\kappa)} - f_{\beta-1/2}^{(\kappa)}), \quad (\overline{f}^x)_\beta^{(\kappa)} = \frac{1}{2}(f_{\beta+1/2}^{(\kappa)} + f_{\beta-1/2}^{(\kappa)}) \tag{5}$$

We note that the differences and averages are defined at intermediate grid locations as compared with f. Difference and average operators with respect to the other coordinate, t, are defined correspondingly. It is easily shown that these operators are commutative in all combinations. To abbreviate the expressions further we also group terms of identical indices inside square brackets, leaving the superscript and subscript outside the right bracket.

A generic FD method will be applied to all Boussinesq formulations [19, 23]. It is defined on a temporally staggered grid, whereas the spatial grid is staggered, too, when u is used as primary unknown. Hence, the unknowns are $\eta_j^{(n)}$ and either $u_{j+1/2}^{(n+1/2)}$ or $\phi_j^{(n+1/2)}$. A sketch of the grid is found in Figure 2. The discrete equations are designed with solely symmetric differences or averages. For the equation of continuity we have

$$[\delta_t \eta = -\delta_x Q]_j^{(n+1/2)} \tag{6}$$

where

$$[Q = hu + \mu^2 Q_1]_{j+1/2}^{(n+1/2)} \quad \text{or} \quad [Q = \overline{h}^x \delta_x \phi + \mu^2 Q_1]_{j+1/2}^{(n+1/2)}$$

We assume that the depth is independent of time and that values for h is available at the semi-integral and integral locations for velocity and potential formulations, respectively. The explicit numeric representation of Q_1 will be given with the descriptions of the Boussinesq formulations. The FD version of the momentum equation reads

$$[\delta_t u = -\delta_x \eta + \mu^2 D_u]_{j+1/2}^{(n)} \tag{7}$$

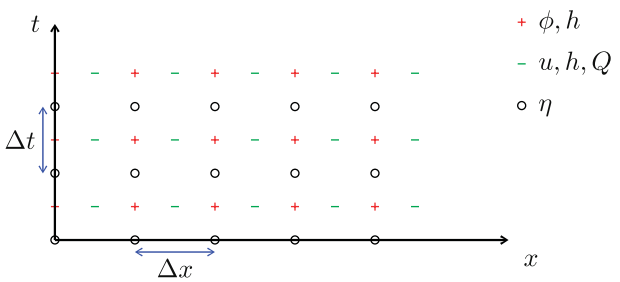

Figure 2. Node distribution in the x, t plane for the generic mid-point method. Each method employes either ϕ or u as unknown. The depth is then specified at the same spatial cite as the employed one.

DOI: 10.1002/fld

Table II. Discrete representations of the μ^2 terms for the different Boussinesq formulations.

Standard velocity formulation	$Q_1=0$
Averaged velocity	$D_u=\frac{1}{2}h\delta_x(\delta_x(h\delta_t u))-\frac{1}{6}h^2\delta_x^2\delta_t u$
Generalized velocity formulation	$Q_1=h\left(\frac{1}{2}z_\alpha^2-\frac{1}{6}h^2\right)\delta_x^2 u+h\left(z_\alpha+\frac{1}{2}h\right)\delta_x^2(hu)$
Velocity at $z=z_\alpha(x,y)$	$D_u=-z_\alpha\delta_x(\delta_x(h\delta_t u))-\frac{1}{2}z_\alpha^2\delta_x^2\delta_t u$
Standard potential formulation	$Q_1=\overline{h}^x\left(\frac{1}{6}\delta_t\overline{\eta}^x-\frac{1}{3}\delta_x h\delta_x\phi\right)\delta_x h$
Averaged potential	$D_\phi=\frac{1}{2}h\delta_x(\overline{h}^x\delta_x\delta_t\phi)-\frac{1}{6}h^2\delta_x^2\delta_t\phi$
Mild-slope formulation	$Q_1=0$
Averaged potential	$D_\phi=h^2\left(\kappa\delta_x^2\eta+\left(\frac{1}{3}+\kappa\right)\delta_x^2\delta_t\phi\right)$
Generalized potential formulation	$Q_1=\overline{h}^x\delta_x\left(z_\alpha\delta_x(\overline{h}^x\delta_x\phi)+\frac{z_\alpha^2}{2}\delta_x^2\phi\right)s+\frac{(\overline{h}^x)^2}{2}\delta_x^2(\overline{h}^x\delta_x\phi)-\frac{(\overline{h}^x)^3}{6}\delta_x^3\phi$
Potential at $z=z_\alpha(x,y)$	$D_\phi=-\frac{1}{2}z_\alpha^2\delta_x^2\delta_t\phi-z_\alpha\delta_x(\overline{h}^x\delta_x\delta_t\phi)$

while the Bernoulli equation takes of the form

$$[\delta_t\phi+\eta-\mu^2 D_\phi=0]_j^{(n)} \tag{8}$$

The elaborate forms of the discrete dispersion terms are given in Table II. In the hydrostatic approximation $\mu\to 0$ we may make the identification $[u=\delta_x\phi]_{j+1/2}^{(n+1/2)}$. Then the two representations of Q below (6) become identical and application of δ_x to (8) reproduces (7). For constant depth a similar equivalence exists also for certain Boussinesq equations. Hence, in principle we apply the same model to formulations based on both potential and velocity.

For generality a finite element method is also tested (Appendix A.1).

3.3. Separation of variables

We employ linear equations with time-independent bathymetry. Hence, there exist a separated solution of the form

$$\eta(x,t)=\hat{\eta}(x)\mathrm{e}^{\mathrm{i}\omega t},\quad u(x,t)=\hat{u}(x)\mathrm{e}^{\mathrm{i}\omega t},\quad \phi(x,t)=\hat{\phi}(x)\mathrm{e}^{\mathrm{i}\omega t} \tag{9}$$

The quantity ω may be real or complex and will generally be found from an eigenvalue problem in the subsequent applications. In the linearized Boussinesq equations the separation will simply result in the substitution $\partial u/\partial t\to \mathrm{i}\omega\hat{u}$, etc.

For the discrete equations the separation of variables will yield similar results as for the PDEs, but with ω replaced by $\tilde{\omega}=2\sin(\frac{1}{2}\omega\Delta t)/\Delta t$, where Δt is the time increment. Moreover, elimination may yield a difference equation in a single unknown, only, just as for the PDEs. Observing $D_u\to \mathrm{i}\tilde{\omega}\hat{D}_u$ and $Q\to\hat{Q}$ the single discrete equation for the velocity-based formulations becomes

$$[\tilde{\omega}^2(\hat{u}-\mu^2\hat{D}_u)+\delta_x^2\hat{Q}=0]_{j+1/2} \tag{10}$$

For the standard formulation this yields a three-diagonal set of equations, whereas the number of diagonals become 5 for the generalized formulation.

DOI: 10.1002/fld

For the standard, the mild-slope and the generalized potential formulations we obtain, respectively,

$$\tilde{\omega}^2\left(\hat{\phi}-\mu^2\hat{D}_\phi-\frac{\mu^2}{6}\delta_x(\overline{h}^x\delta_x h\overline{\hat{D}_\phi}^x)\right)+\delta_x\left(\overline{h}^x\delta_x\hat{\phi}-\frac{\mu^2}{3}\overline{h}^x(\delta_x h)^2\delta_x\hat{\phi}\right)=0 \tag{11}$$

$$\tilde{\omega}^2(\hat{\phi}-\mu^2h^2(\tfrac{1}{3}+\kappa)\delta_x^2\hat{\phi})+\delta_x\hat{Q}-\kappa\mu^2h^2\delta_x^3\hat{Q}=0 \tag{12}$$

$$\tilde{\omega}^2(\hat{\phi}-\mu^2\hat{D}_\phi)+\delta_x\hat{Q}=0 \tag{13}$$

All of these yield equation sets with five diagonals, except (12) for the special case of $\kappa=0$.

4. DISPERSION PROPERTIES AND STABILITY IN CONSTANT DEPTH

In constant depth we have spatial distributions of the form

$$\hat{*}=A_*\mathrm{e}^{\mathrm{i}k}$$

with $*$ indicating η, u or ϕ. When the above expression is inserted in Boussinesq equations where the temporal factor is already separated we find the dispersion relation in terms of ω and k. The generic relation reads

$$\frac{\omega^2}{hk^2}=\frac{1+\mu^2\kappa h^2k^2}{1+\mu^2(\frac{1}{3}+\kappa)h^2k^2} \tag{14}$$

while the amplitudes obey

$$A_\eta=\mathrm{i}\omega\left(1+\mu^2\left(\frac{1}{3}+\kappa\right)(kh)^2\right)A_\phi,\quad A_\eta=\frac{\omega}{k}\left(1+\mu^2\left(\frac{1}{3}+\kappa\right)(kh)^2\right)A_u \tag{15}$$

For generality we have retained the constant value of the depth, h, in these relations. The relations between κ and the parameters of the different Boussinesq formulations are listed in Table III. In terms of κ a particularly favorable dispersion relation is obtained with $\kappa=0.057$, which corresponds to $z_\alpha/h=-0.531$ in the generalized formulation and $\kappa=0.057$ in the mild-slope formulation based on the potential. Moreover, we observe that equations leading to negative κ are unstable for large k.

In case of constant depth the discrete equations invariably involve central differences for the derivatives, since all averages vanish. In comparison with the separation of the differential equations, ω is replaced by $\tilde{\omega}$ and k is replaced by

$$\tilde{k}\equiv\frac{2}{\Delta x}\sin\left(\frac{k\Delta x}{2}\right)$$

Table III. Values of κ for the Boussinesq formulations encountered in this paper.

Formulation	κ
Standard formulations based on depth averaged quantities	0
Mild-slope formulation	κ
Generalized formulations	$-\frac{1}{3}-\frac{z_\alpha^2}{2h^2}-\frac{z_\alpha}{h}$

DOI: 10.1002/fld

because δ_x yields the factor $\mathrm{i}\tilde{k}$. This means that the expressions (14) and (15) will apply to discrete case after the substitution $\omega \to \tilde{\omega},\ k \to \tilde{k}$. This leads to a CFL-type stability criterion of the form

$$h\Delta t^2 \leqslant \Delta x^2 + \frac{\mu^2 h^2 \Delta x^2}{\frac{3}{4}\Delta x^2 + \kappa \mu^2 h^2} \tag{16}$$

corresponding to $1/2\Delta t|\tilde{\omega}|<1$. Our search for unstable modes due to bathymetry will be concerned with complex $\tilde{\omega}$. Thus, there is no possibility for confusing such instabilities with violation of (16).

For both the differential and difference equations the relations between ω and k and between the amplitudes are valid also for complex ω and k, which appear subsequently. We then define $\omega = \gamma + \mathrm{i}\sigma$. In particular, we will encounter purely imaginary values of ω that must be related to imaginary wave numbers. For $\kappa = 0$ (the standard Boussinesq formulations) the discrete dispersion relation then gives

$$\tilde{k}^2 = -\frac{\hat{\sigma}^2}{h + \dfrac{\mu^2}{3}(\hat{\sigma}h)^2} \tag{17}$$

where

$$\hat{\sigma} = \frac{2}{\Delta t}\sinh\left(\frac{\sigma \Delta t}{2}\right)$$

Equation (17) implies a pair of purely imaginary wave numbers

$$k = \mathrm{i}k_I = \pm \mathrm{i}\frac{2}{\Delta x}\operatorname{arc\,sinh}(\tilde{k}\Delta x/2) \tag{18}$$

Hence, we have either exponential growth or decay in space. On the other hand, $\kappa>0$ (the improved Boussinesq formulations) yields a bi-quadratic equation for $\tilde{k}$ with two pairs of k_I as solutions. We label those values as $\tilde{k}_{I1}$ and $\tilde{k}_{I2}$, respectively, and find for $q = 1, 2$

$$\begin{aligned}\tilde{k}_{Iq} &= \frac{2}{\Delta x}\sinh\left(\frac{k_{Iq}\Delta x}{2}\right) \\ &= (2\kappa h(\mu h)^2)^{-1/2}\left(-\left[(\mu\hat{\sigma}h)^2\left(\frac{1}{3}+\kappa\right)+h\right]\right. \\ &\quad \left. +(-1)^q\left\{\left[(\mu\hat{\sigma}h)^2\left(\frac{1}{3}+\kappa\right)+h\right]^2 - 4\kappa h(\mu\hat{\sigma}h)^2\right\}^{1/2}\right)^{1/2}\end{aligned} \tag{19}$$

The existence of two imaginary wave numbers leading to the same imaginary ω, for $\kappa>0$ has bearing for the subsequent analysis and the interpretation of unstable modes.

DOI: 10.1002/fld

5. TEST PROBLEMS AND SOLUTION PROCEDURES

5.1. Definition of test geometries

In a discrete context the simplest non-uniform bathymetry to analyze is a sawtooth bottom where a flat seabed is overlain with a periodic variation on grid scale

$$h_j = 1 + (1 - h_\mathrm{m}) K_j, \qquad K_j \equiv (-1)^j \tag{20}$$

where the minimum depth, h_m, must be less than unity (Figure 3). An inspection of the discrete equations for $\hat{u}$ or $\hat{\phi}$ then reveals that there are two families of node values, associated with even and odd j, respectively, that inherit trigonometric/exponential solutions with different amplitudes.

In principle, eigensolutions in closed basins with impermeable side walls, or inifinite media with a confined patch of non-uniform bottom, can be found for any depth profiles. Herein, we focus on two simple depth configurations, namely a shelf and a sea mount. In both cases the depth is defined by a simple formula. The shelf is defined according to

$$h(x) = \begin{cases} 1, & -\dfrac{W}{2} \leqslant x \leqslant -\dfrac{L}{2} \\ \dfrac{1}{2}\left(1 + h_\mathrm{m} + (1 - h_\mathrm{m}) \cos\left(\dfrac{\pi x}{L}\right)\right), & |x| < \dfrac{L}{2} \\ h_\mathrm{m}, & \dfrac{L}{2} \geqslant x \geqslant \dfrac{W}{2} \end{cases} \tag{21}$$

We observe that $\Delta x \leqslant L/2$ corresponds to a step-shelf. For a sea mount of width L, basin width W, and minimum depth h_m, the depth $h(x)$ is given by

$$h(x) = \begin{cases} 1 - (1 - h_\mathrm{m}) \cos(\pi x / L)^2, & |x| < \dfrac{L}{2} \\ 1, & \dfrac{W}{2} \leqslant |x| \geqslant \dfrac{L}{2} \end{cases} \tag{22}$$

We observe that the expression yields a one-point spike when $\Delta x \leqslant L/2$ and there is a grid node at $x = 0$ (see Figure 5).

A definition sketch of a finite width basin is found in Figure 4.

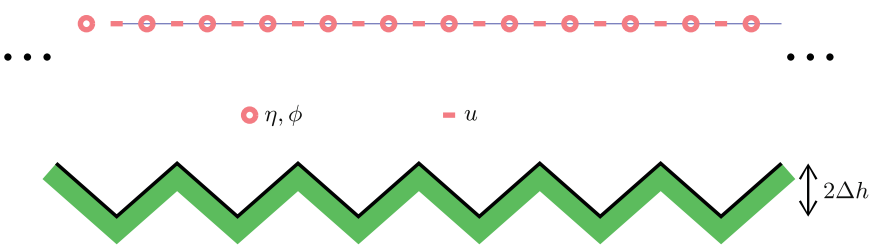

Figure 3. Definition sketch of configuration with sawtooth boundary. The half height of the bottom variations is $\Delta h = 1 - h_\mathrm{m}$ and the depth corresponds to a formulation with velocities as unknowns.

DOI: 10.1002/fld

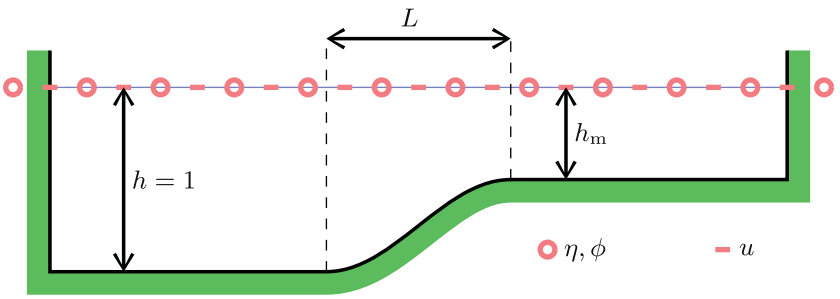

Figure 4. Definition sketch of finite basin with shelf. In a given method we either have velocity nodes at the boundary or fictitious potential nodes half a grid increment beyond the boundary.

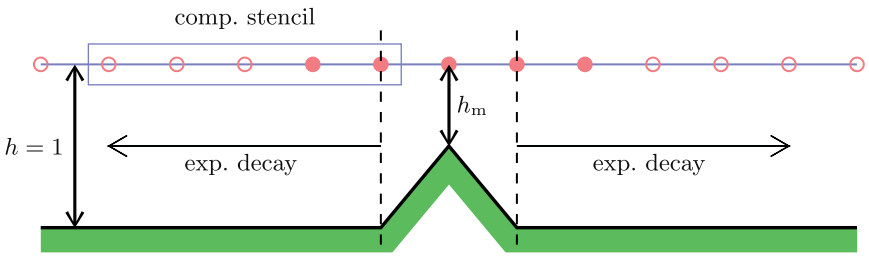

Figure 5. Spike geometry. The centers of the computational stencils that involve the spike are marked by bullets, while the other nodes are circles. The rectangle contains the innermost computational stencil with exclusively unitary depth.

5.2. *The eigenvalue problems*

Below, we present methods for finding eigenvalues and eigenvectors for time separated Boussinesq equations. All the discrete eigenmodes are tested for correctness and accuracy by substituting into the respective difference versions of the Boussinesq equations.

5.2.1. The sawtooth bottom. The sawtooth bottom configuration is set aside from the others since neither the medium nor the variable depth region are confined. A convenient representation of the discrete quantities for this case is

$$\hat{u}_j = A\mathrm{e}^{\mathrm{i}kj\Delta x} + BK_j\mathrm{e}^{\mathrm{i}kj\Delta x} \tag{23}$$

where A and B are constants. We observe that $\hat{u}$ is made up from two independent waveforms. Naturally, a similar form to (23) may be invoked for $\hat{\phi}$ or $\hat{\eta}$. The form (23) is ambiguous. Given that the expression defines a solution, this may also be written as $\hat{u}_j = \overline{B}\mathrm{e}^{\mathrm{i}\hat{k}j\Delta x} + \overline{A}K_j\mathrm{e}^{\mathrm{i}\hat{k}j\Delta x}$, with $\hat{k} = \pi/\Delta x - k$ and the bar denoting complex conjugation. Uniqueness is not required in the present context, but could have been assured by claiming $k\Delta x \leqslant 1/2\pi$.

Selecting the Nwogu formulation as an example, (20) and (23) are inserted into (10). The z_α may be chosen either as a constant or as a constant times the depth, h. We have preferred the latter option to be in line with the common application of these equations. The difference operators may

DOI: 10.1002/fld

be replaced by different factors for the two waveforms, while the waveforms will couple through the multiplications with the depth. The result will be a 2×2 equation set for A and B, where the coefficients depend on $h_{\mathrm{m}}, z_\alpha/h, \Delta x, k$ and $\tilde{\omega}^2$. Existence of a non-trivial solution then requires zero determinant, which yields a bi-quadratic equation for $\tilde{\omega}$, with two pairs of solutions. The solutions within each pair have opposite signs, corresponding to the opposite directions of wave advance or growth/decay, while the two pairs inherit different relations between A and B and thus different overall waveforms. In principle the bi-quadratic equation for $\tilde{\omega}$, found for a sawtooth bottom, can be solved in closed form to give $\tilde{\omega}(h_{\mathrm{m}}, k, \Delta x, z_\alpha/h)$. Unfortunately, the expressions are generally too lengthy to be helpful in further analysis. Instead, instability projection maps are obtained by selecting two parameters from the list and then searching a large number of combinations of the remaining ones for instabilities. If one or more instabilities are found for a given pair it is marked as unstable. Naturally, only a finite discrete sample of combinations may be investigated in this manner, and there is no guarantee against losing isolated or very localized instabilities. On the other hand, this is not likely as long as the resulting maps are smooth, dominated by large scale features and are insensitive to a refinement of the sampling.

5.2.2. Finite width basins. At the end-walls of a finite basin we implement either zero velocity or a symmetry condition for ϕ, depending on the formulation. After elimination of η (see Section 3.3) the separated Boussinesq-type equations yield an eigenvalue problem for $\tilde{\omega}$ of the form

$$(\mathbb{A}-\tilde{\omega}^2\mathbb{B})\boldsymbol{\psi}=0 \tag{24}$$

where $\mathbb{A}$ and $\mathbb{B}$ are banded coefficient matrices with bandwidths $2n+1$, with $n=1$ for the standard and mild-slope formulations, and $n=2$ for the generalized formulations. The vector $\boldsymbol{\psi}$ contains the values of $\hat{\phi}_j$ for potential formulations, or $\hat{u}_{j+1/2}$ for the velocity-based formulations.

The matrices of the generalized eigenvalue problem, (24), are neither symmetric nor positive semi-definite. Eigenvalues and vectors are obtained by reducing the problem to a standard one by inverting $\mathbb{B}$, invoking the MATLAB function eig, which again employs the LAPACK library [24]. Then, the LAPACK solver DGGEV is used with a generalized Schur decomposition. In the first step the eigenvalue problem loses both the band structure and the sparsity, which makes the subsequent steps computationally heavy.

5.2.3. Localized bottom gradients in infinite media. Naturally, the boundaries of finite basins may influence the eigenmodes substantially. Thus, it is desirable to seek unstable modes in the absence of lateral boundaries, meaning an infinite domain.

First we assume that we have a confined region of non-constant depth, adjoined by two semi-infinite horizontal planes. Next, we observe that in the far-field, well into the regions of constant depth, the field variables vary exponentially, i.e. $\hat{\eta}, \hat{u}, \hat{\phi} \sim \exp(\mathrm{i}kx)$, where the imaginary part of k must correspond to decay in infinity. The experience from the closed basin solutions discussed below then lead us to assume purely imaginary k, that relates to the eigenvalue ω according to the relations (18), when κ in (14) equals zero, or (19) otherwise. In the latter case we must combine two exponentials in the far field. Naturally, the exponential solutions cannot apply throughout the region of variable depth. On the other hand, they often apply to the points at the margins of a shoal or a slope.

We now look more closely at the generalized potential model, (13), with a spike geometry. The computational stencil for this model involves five nodes. A definition sketch is shown in Figure 5.

DOI: 10.1002/fld

First we consider a stencil located far from the spike, containing nodes with unitary depth only. In this stencil the solution is a superposition of two exponential functions as stated above. Next, we select the stencil that is located one grid point closer to the spike, implying that the two stencils have 4 overlapping nodes. Hence, the difference equation implies that the value at the fifth node in the second stencil is also given by the same exponentials. Performing this operation repeatedly, we realize that the exponential form applies to all nodes that may be linked to the far field through computational stencils that are unaffected by depth gradients. For the generalized potential model we then reach the nodes adjacent to the spike, while the value at the spike itself is not given by the exponential expression. However, there are five computational stencils that involve the spike and these then provide 5 linear equations for 5 unknowns, namely the value at the spike and 4 amplitudes for the exponentials (2 to each side). If we assume symmetry, the number of unknowns is reduced to 3. Requirement of zero determinant then yields an equation for $\tilde{\omega}$ that is highly non-linear due to the relation between the complex wave numbers of the exponentials and $\tilde{\omega}$. The eigenvalue, $\tilde{\omega}$, is then found using a zero point solver [25]. Normalizing the eigenvector by setting $\hat{\phi}$ at the spike node to unity, for instance, a discrete solution for $\hat{\phi}$ is then readily obtained. In principle the procedure may be applied for sea mounts extending any number of nodes.

A step-shelf may be treated in a similar manner as the spike. Again, the solution in the far-fields is given by exponentials with wave numbers that are linked to ω through the discrete dispersion relation, inserted $h=1$ in the deep region and $h=h_{\mathrm{m}}$ on the shelf. Naturally, this time there is no symmetry in the solution, but we still end up with small linear equation systems for nodes in the vicinity of the step and the amplitudes in the far field.

The spike and step-shelf solutions are obtained correspondingly for the other methods and on a few occasions we are even able to prove analytically that all modes are stable (see Appendix A.3).

6. RESULTS

6.1. *Classification of instabilities*

In all cases each mode is linked to an $\tilde{\omega}^2$, either from an algebraic equation or from the numerical solution of a generalized eigenvalue problem. Unstable wave modes may then appear in three manners.

(I) $\tilde{\omega}^2<0$. The 'frequency', ω, will then be purely imaginary and the solutions will thus grow/decay exponentially without propagation.

(II) We find a complex conjugate pair for $\tilde{\omega}^2$. The solutions will then both grow/decay and propagate. This type of instability is not revealed using the methods for infinite basins.

(III) Only real solutions are found for $\tilde{\omega}$, but two of them yield $1/2\Delta t|\tilde{\omega}|>1$ and complex ω. This corresponds to a CFL criterion, which is modified compared with (16), but this kind of instability may anyhow be avoided for a sufficiently small Δt.

Sometimes we find imaginary $\tilde{\omega}$ with small growth rates from the numerical eigenvalue solutions. As a rule we reconstructed the complete discrete fields, $\eta_j^{(n)}$ and $u_{j+1/2}^{(n+1/2)}$ or $\phi_j^{(n+1/2)}$ and inserted those into the finite difference equations. Of course, due to round off errors and inaccuracies in the eigenvalue solutions the difference equations are not exactly fulfilled, but we generally find residuals of order 10^{-10}, or smaller, with 64 bits arithmetics. For the generalized potential formulation, in particular, the residuals are sometimes larger than 10^{-6}. Moreover, we also observe

DOI: 10.1002/fld

Table IV. e-folding times, t_e^* for some depths h^* and growth rates σ.

Growth rate σ	$h^*=200$ m	$h^*=1000$ m	$h^*=5000$ m
10^{-5}	125 h 25 min	280 h 27 min	627 h 6 min
10^{-4}	12 h 32 min	28 h 2 min	62 h 42 min
10^{-2}	7 min 31 s	16 min 49 s	37 min 37 s
1	4.5 s	10 s	23 s

the growth of the reconstructed fields during a large number of time steps. For solutions of large eigenvalue problems, with small but finite growth rates ($0<\sigma<10^{-6}$), absence of growth in the time stepping is sometimes observed. It is presumed that the low values of σ are erroneous results of the eigenvalue solver. Therefore, to provide reasonable stability limits for the models investigated, we apply $\sigma=10^{-5}$ as a lower bound for eigensolutions that are reckoned as unstable modes.

To illustrate the significance of small growth rate we define a e-folding time according to

$$t_e^*=\sqrt{\frac{h^*}{g}}\sigma^{-1} \tag{25}$$

where h^* is a typical depth with dimension. Table IV shows examples of t_e^* for some different depths and growth rates. The depth 200 m is chosen to represent a typical maximum depth near shore or in a fjord, while the depths of 1000 and 5000 m are maximum depths representative for the deep ocean. From Table IV we see that for σ larger than or equal to 1, severe instabilities are introduced. For $\sigma=10^{-2}$, t_e^* is comparable to the wave period of the Indian Ocean tsunami [26] and to characteristic propagation times for the Tafjord [18] case. Thus, such a growth will generally destroy tsunami simulations. Unless large simulation times are considered, the instabilities caused by $\sigma=10^{-4}$ will not influence the results very much; even a small amplification of 10% due to instability for $h^*=200$ m and $\sigma=10^{-4}$ will occur after more than one hour. The table also illustrates that the lower bound growth rate of $\sigma=10^{-5}$ in most cases do not influence tsunami simulations.

6.2. *Wave propagation over a sawtooth bottom*

Only a selection of the methods in Table II has been investigated for the sawtooth configuration (see remarks below).

- *Standard velocity formulation*. The equations for $\tilde{\omega}$ are complex and no attempt has been made to prove stability analytically. However, in accordance with subsequent results for the standard velocity formulation, projection maps reveal no sign of instability.
- *Generalized velocity formulation*. In this case the discrete frequencies depend on z_α/h in addition to h_m, Δx and k. Projection maps for $z_\alpha/h, \kappa$ and $z_\alpha/h, \Delta x$ are given in Figure 6. From the figures we infer that the region with z_α/h close to -0.531, which is of particular interest, is affected by unstable modes of type I, but not of type II. Hence, stability limits are given by $\tilde{\omega}=0$ ($\tilde{\omega}^2$ changes sign), which implies a relation of the kind $\Delta x=\Delta x(z_\alpha/h, k, \kappa)$ that is obtained from a bi-quadratic equation for Δx. A real and positive value for Δx is then a stability limit. To find the wave number yielding the largest unstable Δx value it suffices to

DOI: 10.1002/fld

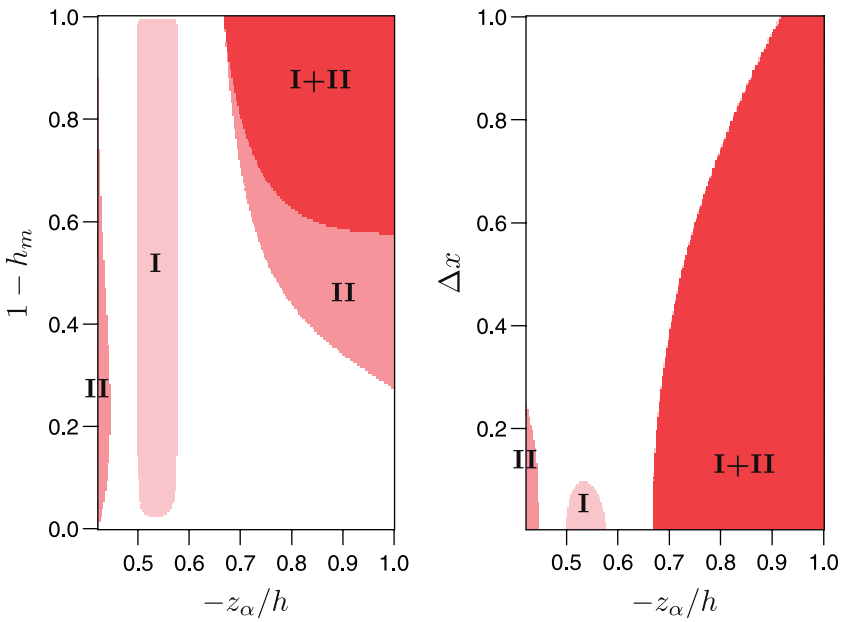

Figure 6. Projection maps for type I and II instabilities. The white regions are stable. We observe that $z_\alpha/h=-0.531$ is within a type I region.

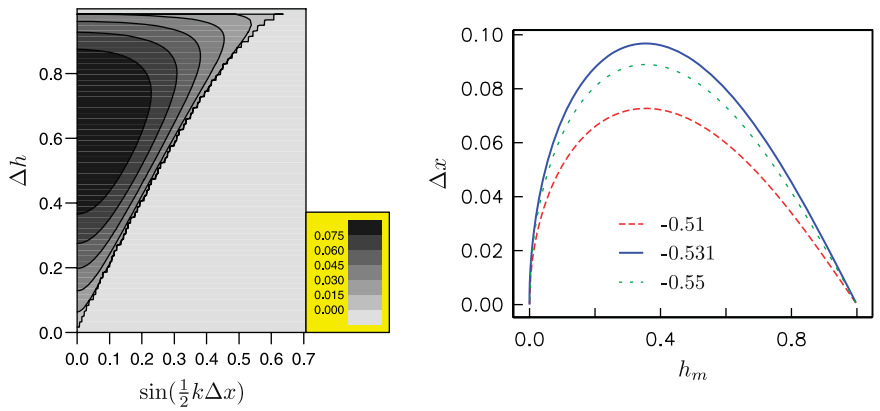

Figure 7. Left panel: contour plot of critical Δx. We observe that for a given Δh the largest Δx is found for $k=0$. Right panel: stability limits marked by values of z_α.

investigate $k\Delta x\leqslant 1/2\pi$ (Section 5.2.1). Figure 7, left panel, then points to $k=0$ and $k=\pi/\Delta x$ and the equation for Δx is reduced to the simple form

$$\Delta x^4-4(\tfrac{1}{2}z_\alpha^2+z_\alpha+\tfrac{1}{3})(\Delta h^2+1)\Delta x^2-(4+8z_\alpha)(z_\alpha^2-1)(\Delta h^2-\Delta h^4)=0$$

DOI: 10.1002/fld

where $\Delta h = 1 - h_{\mathrm{m}}$. A straightforward analysis of the coefficients reveals that positive roots for Δx^2 require $-\frac{1}{\sqrt{3}} < z_\alpha / h < -\frac{1}{2}$, which is consistent with the region of type I instability in Figure 6. Still, as shown in Figure 7, right panel, the largest Δx enabling instability is less than 0.1 for $z_\alpha / h = -0.531$. Considering that the optimized Boussinesq equation is good for wavelengths down to two depths, this is a rather fine resolution.

- *The mild-slope formulation*. For $\kappa = 0$ we may obtain a simple equation for $\tilde{\omega}$ and can prove that there are no unstable modes. Otherwise the expressions again become too lengthy for an analytic approach. However, projection maps show no sign of instability for the mild-slope formulation, with $\kappa < 0.1$.

Instability in the presence of sawtooth bottom may be analyzed correspondingly for the standard and improved potential formulations. However, even though a high relief sawtooth bottom may be relevant for rough discretization of shallow waters, the observed instabilities in Section 2 were strongly localized. Moreover, the sawtooth bottom instabilities are always closely linked to the numerics. We will instead turn the attention to other bottom configurations for which grid refinement can be applied and instabilities inherent in the equations themselves may be addressed.

6.3. Step-shelves and spike geometries

Below, we list findings of instabilities in step-shelf and spike geometries model by model. Projection maps of the maximum growth-rate $\sigma_{\max}$ are displayed, while the shape of the unstable modes are presented in detail in Appendix A.2.

- *Standard velocity formulation.* For the standard velocity model, no unstable modes are found for any depth configuration. In fact, it is proved in Appendix A.3 that the standard velocity formulation is stable for any spike or step-shelf in infinite media.
- *Improved velocity formulation.* Figure 8 (lower panel) shows that small Δx are needed for an instability to arise, and, in addition, that the stability limits are hardly sensitive to the basin width. Moreover, the curves in Figure 8 are similar to those of a sawtooth bottom (Figure 7), but the unstable region is smaller for a single spike, yet the step-shelf has an even smaller unstable area.
- *Generalized velocity formulation with* $z_\alpha / h = \sqrt{\frac{1}{3}} - 1$. Figure 8 (upper left panel) shows that only a small area in the $h_{\mathrm{m}}, \Delta x$ plane is unstable both for a spike and a step. Computations for a spike in an infinite media gave no instabilities, consistent with the findings of type II instabilities only for finite basin widths. Unexpectedly, the unstable solutions are found for values of h_{m} close to 1, meaning small changes in depth. We remark that although the generalized model coincides with the standard model in constant depth for this value of z_α, the stability properties in variable depth are highly different.
- *Generalized velocity formulation with* $z_\alpha / h = -1$. Figure 8 (upper right panel) shows that the unstable solutions appear for small values of h_{m} and Δx. Moreover, the figure shows that the basin width influences the stability markedly. The stability curves are restricted to spike geometries. The step-shelf yields a smaller unstable area (results not shown).
- *Standard potential formulation.* Figure 9 (upper panel) shows different stability limits. For this model the eigenvalues for a step-shelf in an infinite medium are also computed. The stability requirements in Figure 9 all appear to be on the form

$$\Delta x > f(h_{\mathrm{m}}) \tag{26}$$

DOI: 10.1002/fld

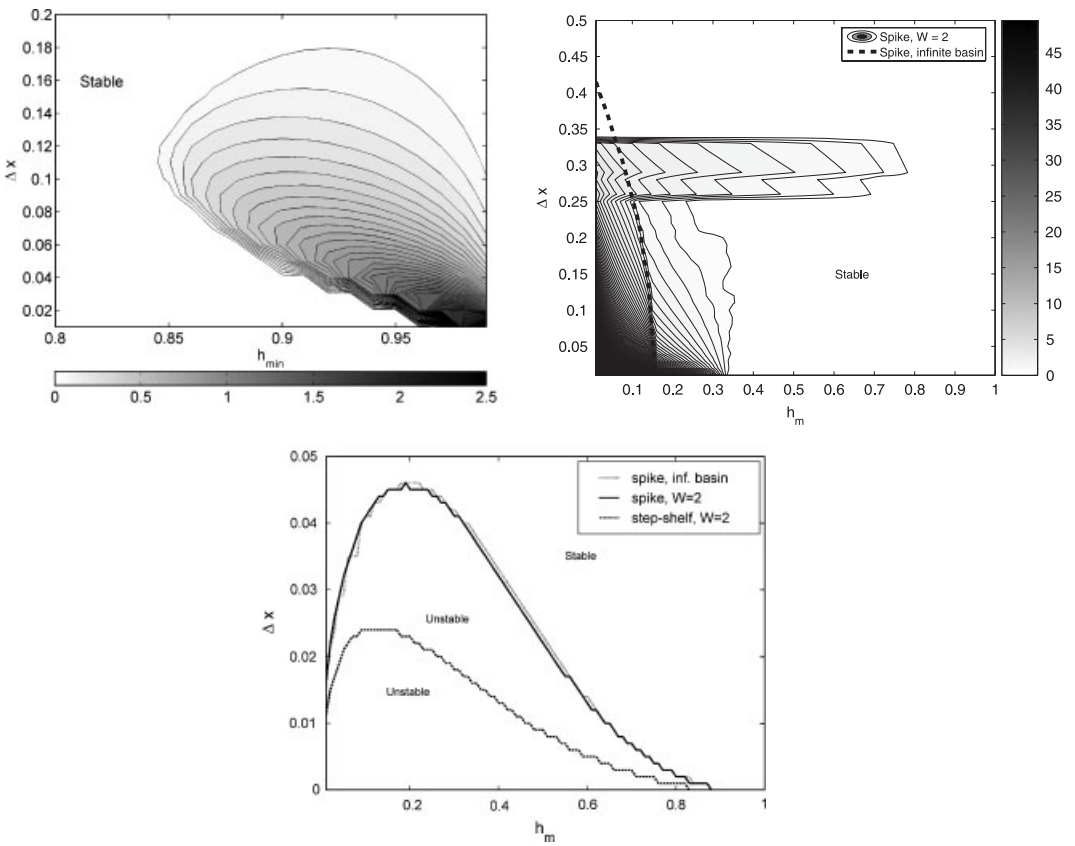

Figure 8. Upper left panel: contour plots of $\sigma_{\max}(h_{\mathrm{m}}, \Delta x)$ for the generalized velocity model (step-shelf geometry), $z_\alpha/h = \sqrt{\frac{1}{3}} - 1$. White color indicates that the model is stable, while gray color indicates instability. The basin width is $W = 2$. Upper right panel: contour plot of $\sigma(h_{\mathrm{m}}, \Delta x)$ for the generalized velocity model, $z_\alpha/h = -1$. White color indicates that the model is stable, while gray color indicates instability. The geometry is a step with a basin width $W = 2$. The dashed line indicates the stability limit for a spike geometry in a infinite basin. Lower panel: stability limits for improved velocity model. The solid line shows the stability limit for an infinite basin with a spike, the dotted line for a spike in a finite basin of $W = 2$ (more or less coinciding with the infinite basin), and the dashed line for step in a finite basin of $W = 2$. The colorbars indicate the values of $\sigma_{\max}$.

for a monotonically decreasing function $f(h_{\mathrm{m}})$. In particular, it has been shown (Appendix A.3) that for spikes and step-shelves no unstable type I modes exists for the standard potential model when

$$\Delta x > \sqrt{\tfrac{1}{3}}(1 - h_{\mathrm{m}}) \quad \text{or} \quad \delta_x h < \sqrt{3} \tag{27}$$

In the rightmost expression the criterion is expressed in terms of the maximum discrete depth gradient. However, for the step-shelf, unstable solutions appear for larger values of Δx than given in Equation (27), owing to the occurrence of type II instabilities. Moreover, it is shown

DOI: 10.1002/fld

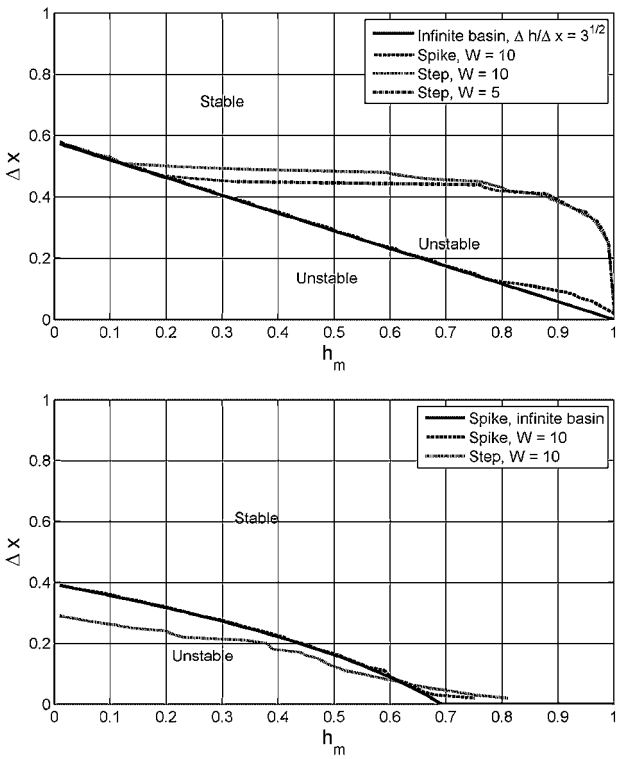

Figure 9. Upper panel: stability limits for standard potential model. The solid line shows the stability limit for an infinite basin for both a spike and a step, the dashed line for a spike in a finite basin of $W=10$ (more or less coinciding with the infinite basin), the dotted line for step in a finite basin of $W=10$, and the dash-dotted line for a step-shelf in a finite basin of $W=5$. Lower panel: stability limits for improved potential model, $z_\alpha/h=-0.531$. The solid line shows the stability limit for an infinite basin with a spike, the dashed line for a spike in a finite basin of $W=10$ (more or less coinciding with the infinite basin), and the dotted line for step in a finite basin of $W=10$.

that the basin width is significant for the stability in step-shelves in finite basins up to about $W=10$.

- *Mild-slope formulation.* The instabilities appearing for the mild-slope model for $\kappa=0.057$ are of type II. Stability curves computed for the mild-slope model display more complicated patterns than for the standard and improved potential models (Figure 10). However, unstable solutions for the mild-slope model appear for small values of h_m only. For the mild-slope model, we also investigated the stability of a finite element discretization (see Appendix A.1). As shown in Figure 10, the finite element method with consistent mass matrix is somewhat more unstable than the corresponding finite difference model. Other basin widths tested gave different but still complicated patterns.
- *Improved potential formulation.* Stability curves for finite and infinite basins for the improved potential model are shown in Figure 9 (lower panel). They display much of the same characteristics as for the standard potential model as given in Equation (26), with the improved potential model being the most stable of the two. The basin width influences stability to a little extent.

DOI: 10.1002/fld

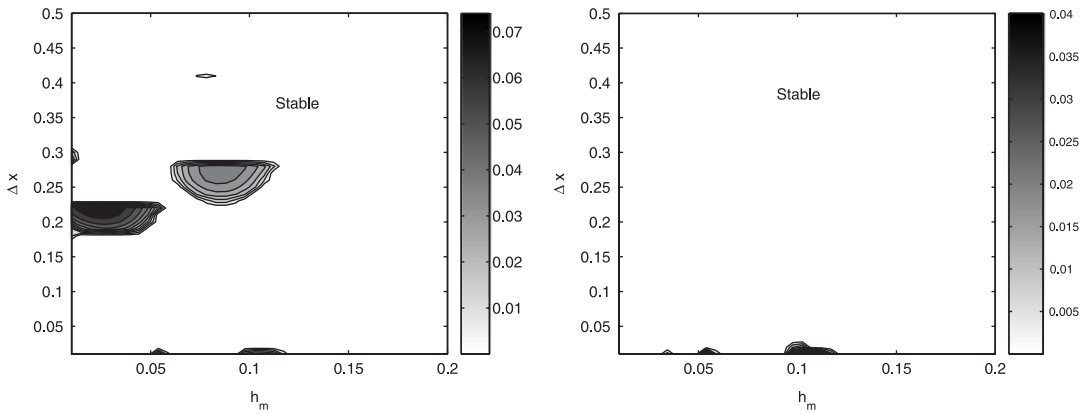

Figure 10. Left panel: contour plot of $\sigma(h_{\mathrm{m}}, \Delta x)$ for the mild-slope model with finite element discretization (consistent mass matrix) and $\kappa = 0.057$. White color indicates that the model is stable, while gray color indicates instability. The geometry is a step-shelf with a basin width $W = 2$. Right panel: contour plot of $\sigma(h_{\mathrm{m}}, \Delta x)$ for the mild-slope model with finite difference discretization and $\kappa = 0.057$. White color indicates that the model is stable, while gray color indicates instability. The geometry is a step-shelf with a basin width $W = 2$. Colorbars indicate the values of $\sigma_{\max}$.

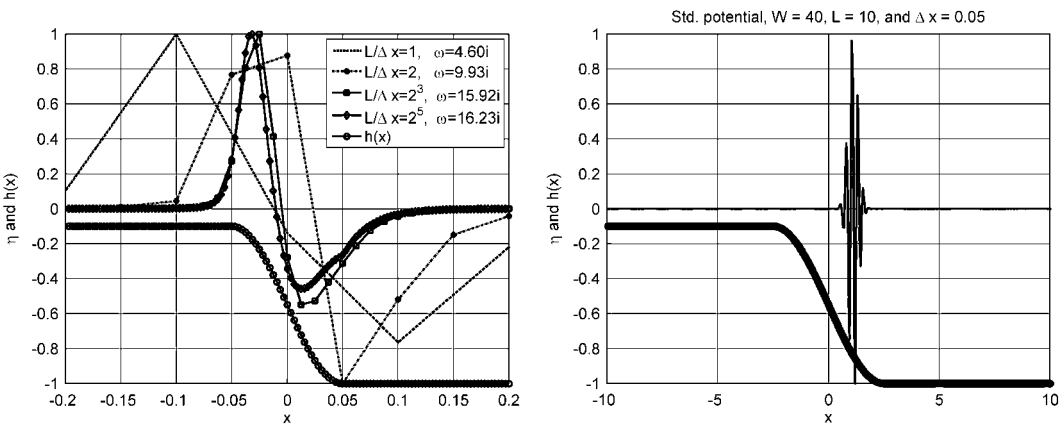

Figure 11. Left panel: surface elevations for different values of Δx for the improved potential model. Shelf with parameters $W = 2$, $L = 0.1$. Right panel: unstable waveforms for a shelf with minimum depths $h_{\mathrm{m}} = 0.1$, using the standard potential model.

6.4. Finite width shelf and sea mount geometries

Next, we explore unstable modes in refined geometries, that is, the shelves and sea mounts defined by Equations (21)–(22). Examples of the variety of the modes are shown in Figure 11. In Appendix A.2, a larger sample of unstable modes are displayed.

- *Standard velocity formulation.* No unstable solutions found.
- *Improved velocity formulation.* The computed maximum growth rates for variable grid resolutions, shown in Figure 12, approach a constant value for decreasing Δx, both for the shelf and the sea mount. We also observe that the unstable waveforms becomes similar as Δx is

DOI: 10.1002/fld

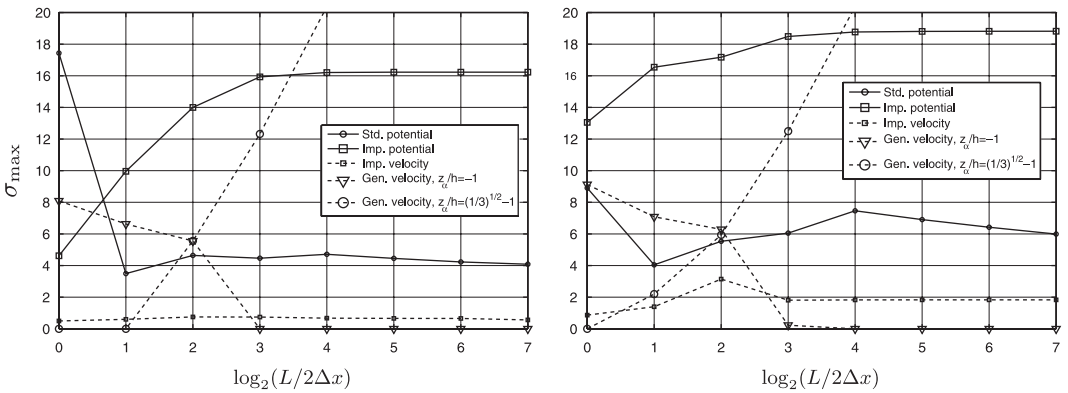

Figure 12. Maximum growth rate $\sigma_{\max}$ for a shelf (left panel) and sea mount (right panel), as a function of the normalized grid size. The minimum depth is $h_m = 0.1$. For the improved velocity model, a basin width of $W = 0.2$ and $L = 0.02$ is applied. For all other models, a basin width of $W = 2.0$ and $L = 0.2$ is applied.

decreased (see Appendix A.2). Combined with the above finding this strongly suggests that the instability is inherent in the equations and will presumably appear for any consistent numerical method without artificial damping.

- *Generalized velocity formulation with* $z_\alpha/h = \sqrt{\frac{1}{3}} - 1$. The computed maximum growth rates for variable grid resolutions, shown in Figure 12, increase for $\Delta x \to 0$, both for the shelf and the sea mount. The instability must therefore be crucially dependent on the numerical method. Naturally, this is no indication of the PDEs themselves being stable.
- *Generalized velocity formulation with* $z_\alpha/h = -1$. Figure 12 shows that $\sigma_{\max}$ vanishes rapidly as $\Delta x \to 0$.
- *Standard potential formulation.* Figure 12 shows that the growth rate $\sigma_{\max}$ attenuates at a moderate rate as Δx decreases, although fairly constant. In addition, the waveforms depend on Δx, as illustrated in A9–A10 in Appendix A.2.
- *Mild-slope formulation.* The irregular patterns of the projection maps in Figure 10 indicate that the instability may be due to the numerical method. In investigations of $\sigma_{\max}$ with similar, but different, values of Δx compared with the ones shown in Figure 12, we find sparsely distributed unstable modes for small Δx (results not shown). However, test simulations show that these modes are indeed unstable.
- *Improved potential formulation.* The grid refinement in Figure 12 shows that $\sigma_{\max}$ approach a constant value for $\Delta x \to 0$, similarly as for the improved velocity model. This suggests that the instabilities observed are inherent in the equations.

7. CONCLUDING REMARKS

Boussinesq models in geometries with large depth gradients are hampered with instabilities, as shown in the example of the Tafjord tsunami.

A range of different Boussinesq models were analyzed in one horizontal dimension, for finite and infinite basins, with bottom variations of sawtooth shape, with single spikes or steps. The

DOI: 10.1002/fld

waveforms of the unstable modes found by numerical eigenvalue analysis were in most cases composed of an oscillating part confined to the variable depth part, and an exponentially decaying part in the area of constant depth. No instabilities were found for LSW or standard Boussinesq equations with velocities. Yet, to various degrees all the other investigated methods displayed instabilities for certain combinations of the parameters.

Grid refinement tests of unstable solutions show that the growth rate of the instabilities converges as $\Delta x \to 0$ for the improved models (both potential and velocity). The waveforms of the corresponding unstable modes are also maintained for $\Delta x \to 0$, which indicate that the instabilities are inherent in the partial differential equations (PDEs). For other models, the trend is different for $\Delta x \to 0$, which indicates that the instability depends genuinely on the numerical method. However, it is still possible, and even likely, that the instabilities are also inherent in the PDEs themselves.

For most models, simple stability relations are found for spike and step-shelf depth configurations. Moreover, in some cases closed-form solutions of the criteria are found, assuming purely imaginary wave numbers and infinite basin widths. In addition, it is found that the basin width can influence stability. The stability criteria show that unstable solutions are generally related to steep gradients. However, even small depth gradients can cause instabilities for some models.

For the improved velocity formulation of [4] we observe instabilities only for steep bottom gradients combined with a small grid increment ($\Delta x/h < 0.1$). Given that the model is valid for wavelengths down to, say, two depths, such increments are probably smaller than what may be used in most applications, at least for computations in two horizontal dimensions. In addition, the mild-slope potential formulation displays good stability properties. In contrast, the other models based on the potential, as well as the generalized velocity model for certain values of z_α/h far from -0.531, were more unstable. The standard potential model, for instance, should not be applied except when encountering gentle bottom variations. However, in such cases the mild-slope version is equally accurate. We also remark that although the standard velocity formulation coincides with the generalized model for $z_\alpha/h = \sqrt{\frac{1}{3}} - 1$ on constant depth, the standard model is always stable in variable depth, whereas the corresponding generalized model is unstable even for small changes in depth, and hence useless for tsunami calculations.

We have found that large depth gradients may cause instabilities in Boussinesq equations. However, related effects may be expected also due to irregular grids and three-dimensional bathymetric features. Such effects may in turn be enhanced by coupling to non-linearities. Whereas a generic finite difference method is applied in this paper, higher-order finite difference, or finite element, methods applied elsewhere in the literature [4, 13, 19, 27–30] may display different stability properties. However, it is emphasized that instabilities probably are inherent in many of the investigated Boussinesq equations themselves and that the problem has been encountered in real simulations. Therefore, modelers are encouraged to investigate stability properties of their Boussinesq techniques carefully.

APPENDIX A

A.1. An example of a finite element discretization

We apply the Galerkin method to the mild-slope formulation on an interval Ω. The equations are multiplied with linear weight functions N_i, integrated over the computational domain (Ω) and

DOI: 10.1002/fld

re-casted into weak form by integration by parts. For the continuity equation we obtain

$$\int_\Omega \left(N_i \mathrm{i}\tilde{\omega}\hat{\eta} - \frac{\mathrm{d}N_i}{\mathrm{d}x} h \frac{\mathrm{d}\hat{\phi}}{\mathrm{d}x} \right) \mathrm{d}x = 0 \tag{A1}$$

while the Bernoulli equation yields

$$\int_\Omega \left(N_i (\mathrm{i}\tilde{\omega}\hat{\phi} + \hat{\eta}) + \mu^2 \frac{\mathrm{d}(N_i h^2)}{\mathrm{d}x} \left(\kappa \frac{\mathrm{d}\hat{\eta}}{\mathrm{d}x} + \mathrm{i}\tilde{\omega} \left(\frac{1}{3} + \kappa \right) \frac{\mathrm{d}\hat{\phi}}{\mathrm{d}x} \right) \right) \mathrm{d}x = 0 \tag{A2}$$

Next, we approximate the surface elevation $\hat{\eta}_j$ and potentials $\hat{\phi}_j$ in terms of piecewise linear trial functions N_j as

$$\hat{\eta} = \sum_j \hat{\eta}_j N_j(x), \quad \hat{\phi} = \sum_j \hat{\phi}_j N_j(x) \tag{A3}$$

By exact integration and assembly of Equations (A1) and (A2) we obtain the discrete continuity equation of the form

$$[\mathrm{i}\tilde{\omega} M \hat{\eta} + \delta_x (h \delta_x \hat{\phi})]_j = 0 \tag{A4}$$

while the discrete Bernoulli equation becomes

$$[\mathrm{i}\tilde{\omega} M \hat{\phi} + M\hat{\eta} - \mu^2 h^2 (\kappa \delta_x^2 \hat{\eta} + \mathrm{i}\tilde{\omega} (\tfrac{1}{3} + \kappa) \delta_x^2 \hat{\phi})]_j = 0 \tag{A5}$$

where the operator M, corresponding to the mass matrix, is defined according to

$$M(*)_j = \frac{m}{6}(*)_{j-1} + \left(1 - \frac{m}{3}\right)(*)_j + \frac{m}{6}(*)_{j+1} \tag{A6}$$

with $*$ indicating $\hat{\eta}$ or $\hat{\phi}$. The factor $m = 1$ is defining a consistent mass matrix and $m = 0$ a lumped (diagonal) mass matrix. The discrete dispersion relation then reads

$$\tilde{\omega}^2 \frac{\tilde{M}}{h\tilde{k}^2} = \frac{\tilde{M} + \mu^2 \kappa h^2 \tilde{k}^2}{\tilde{M} + \mu^2 (\frac{1}{3} + \kappa) h^2 \tilde{k}^2} \tag{A7}$$

for $\tilde{M} = 1 - m\Delta x^2 \tilde{k}^2/6$.

Comparing Equations (6) and (8) with (A4) and (A5), the only difference is the appearance of the mass matrix. By lumping the mass matrix the finite element method gives exactly the same result as the centered difference method, while the methods differ for a consistent mass matrix. In the main text we indicate consistent mass matrices when referring to the finite element method.

A.2. Examples of unstable eigenmodes

A.2.1. Step-shelves and spike geometries. Examples of unstable modes for the simple step-shelf and spike geometries for different models are shown in Figures A1–A8. Type I instabilities ($\omega = \mathrm{i}\sigma$) are found for all models except for the standard velocity model, the generalized velocity model with $z_\alpha/h = \sqrt{\frac{1}{3}} - 1$, and the mild-slope model. For the latter two, only type II instabilities are found. Figures A7–A8 show type II instabilities where combinations of exponential decay and

DOI: 10.1002/fld

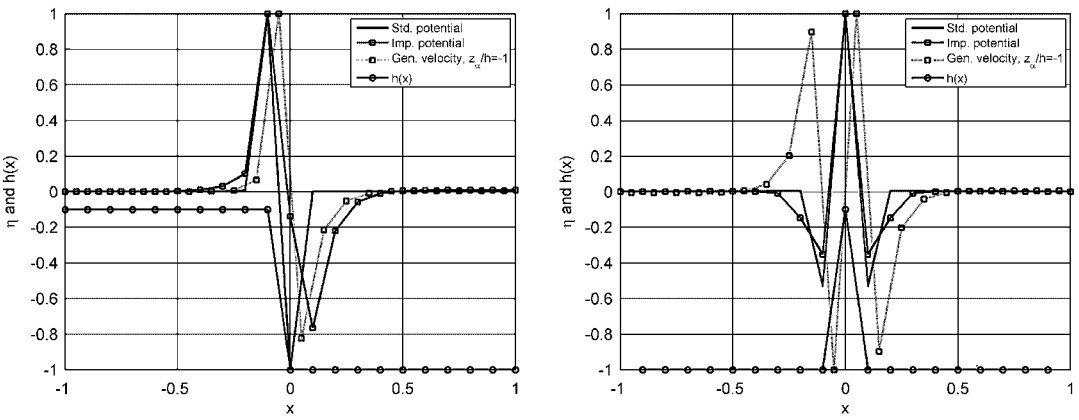

Figure A1. Unstable surface elevation waveforms for different models over a step-shelf (left panel) and a spike (right panel). Basin width $W=2$, minimum depth $h_m=0.1$, step length $L=0.1$, spike width $L=0.2$ and $\Delta x=0.1$.

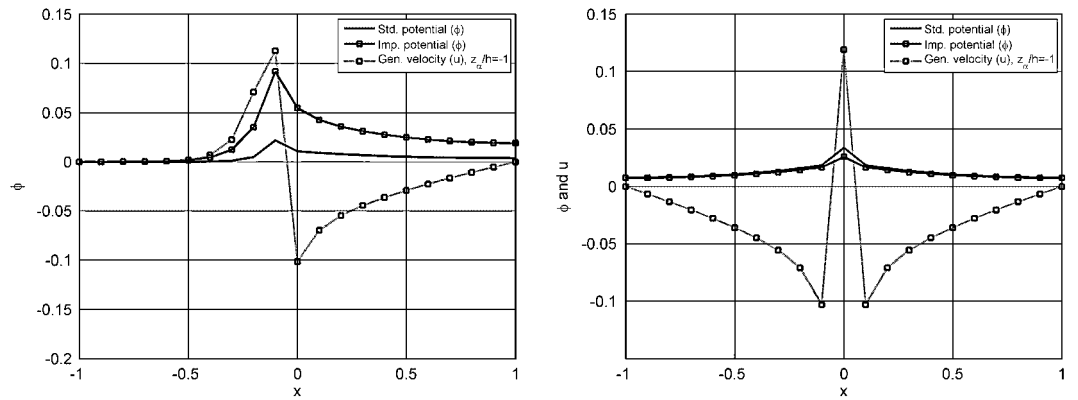

Figure A2. Unstable potential and velocity waveforms for different models over a step-shelf (left panel) and a spike (right panel). Basin width $W=2$, minimum depth $h_m=0.1$, step length $L=0.1$, spike width $L=0.2$ and $\Delta x=0.1$.

oscillations in the far field occur. Small values of Δx and h_m are required to produce unstable modes for the improved velocity model in accordance with Figures A3–A4. Some remarks on the unstable modes are listed below.

- *Standard velocity formulation.* No unstable waveforms found.
- *Improved velocity formulation.* The waveforms of η are characterized by a rather abrupt change close to the step and spike, whereas the velocities display smoother transitions. Consistent with the observation for the sawtooth geometry, the unstable modes are type I. However, slow exponential decay linked to relatively small growth rates causes the waveform of η to appear as almost horizontal. We also note that the waveforms for the spike are antisymmetric for η and symmetric for u.

DOI: 10.1002/fld

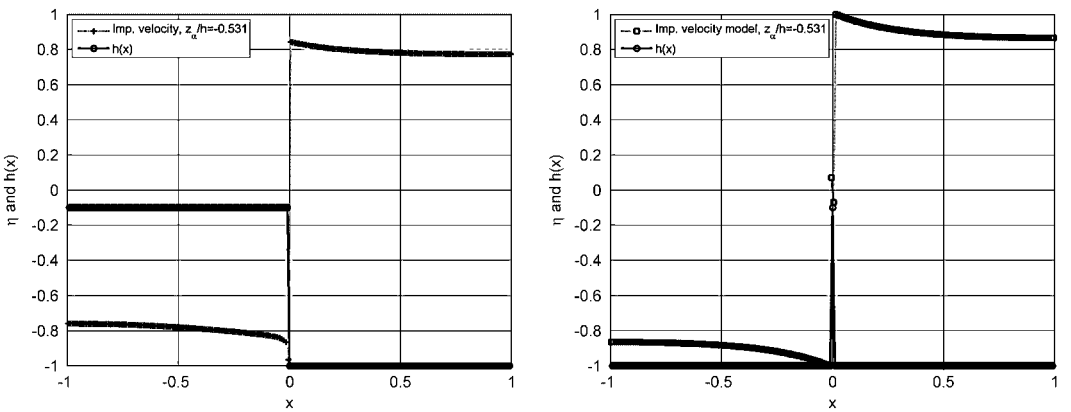

Figure A3. Unstable surface elevation waveforms for the improved velocity model over a step-shelf (left panel) and a spike (right panel). Basin width $W=2$, minimum depth $h_{\mathrm{m}}=0.1$, step length $L=0.01$, spike width $L=0.02$, and $\Delta x=0.01$.

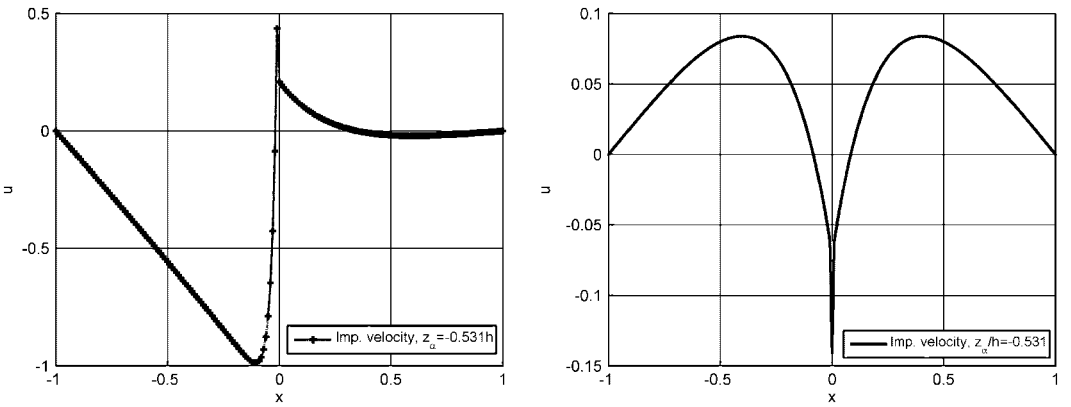

Figure A4. Unstable velocity waveforms for the improved velocity model over a step-shelf (left panel) and a spike (right panel). Basin width $W=2$, minimum depth $h_{\mathrm{m}}=0.1$, step length $L=0.01$, spike width $L=0.02$, and $\Delta x=0.01$.

- *Generalized velocity formulation with* $z_\alpha/h=\sqrt{\frac{1}{3}}-1$. The modes are of type II; however, the oscillations are not conspicuous from Figures A5–A6 as wavelengths are large.

A.2.2. Finite width shelf and sea mount geometries. Examples of unstable wave shapes are shown in Figures A9–A12. They appear in many varieties, displaying smooth wave shapes, as well as spatial oscillations on the grid scale. Unstable modes are displayed for values of L/h_{m} up to 5, and

DOI: 10.1002/fld

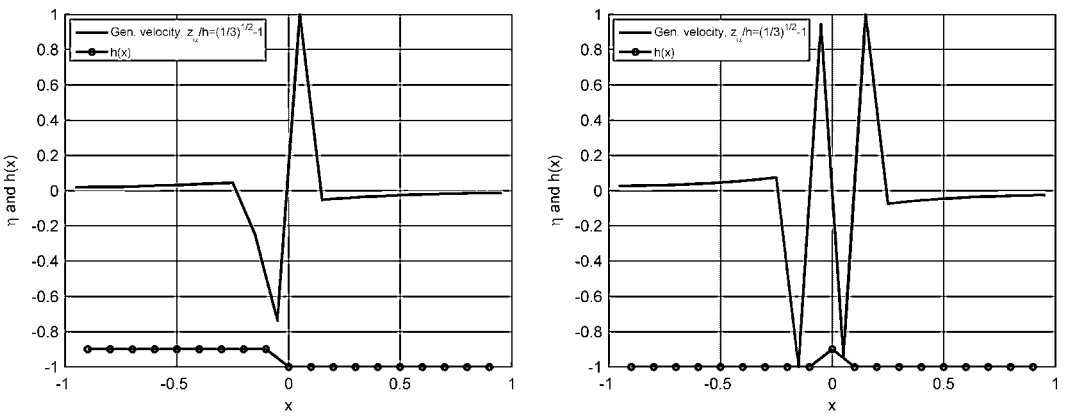

Figure A5. Unstable surface elevation waveforms for the generalized velocity model with $z_\alpha/h=\sqrt{\frac{1}{3}}-1$ over a step-shelf (left panel) and a spike (right panel). Basin width $W=2$, minimum depth $h_m=0.9$, step length $L=0.1$, spike width $L=0.2$, and $\Delta x=0.1$.

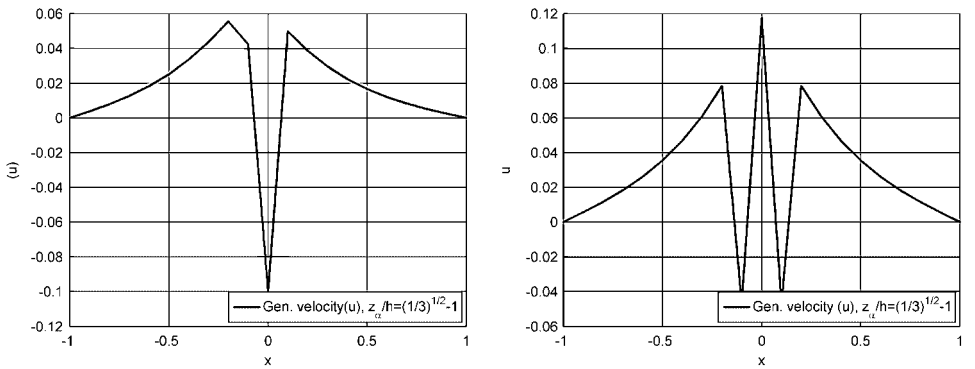

Figure A6. Unstable velocity waveforms for the generalized velocity model with $z_\alpha/h=\sqrt{\frac{1}{3}}-1$ over a step-shelf (left panel) and a spike (right panel). Basin width $W=2$, minimum depth $h_m=0.9$, step length $L=0.1$, spike width $L=0.2$, and $\Delta x=0.1$.

are also found for even larger values of L/h_m (results not shown). For the improved models, we find that the modes appear fairly similar for different values of Δx as shown in Figures A11–A12, converging to smooth wave shapes as $\Delta x \to 0$. Some model-dependent remarks on the unstable modes are listed below.

- *Generalized velocity formulation with* $z_\alpha/h=\sqrt{\frac{1}{3}}-1$. Figures A9–A10 show that the unstable modes display short spatial oscillations on the grid scale, and that the waveforms depend on the grid resolution.

DOI: 10.1002/fld

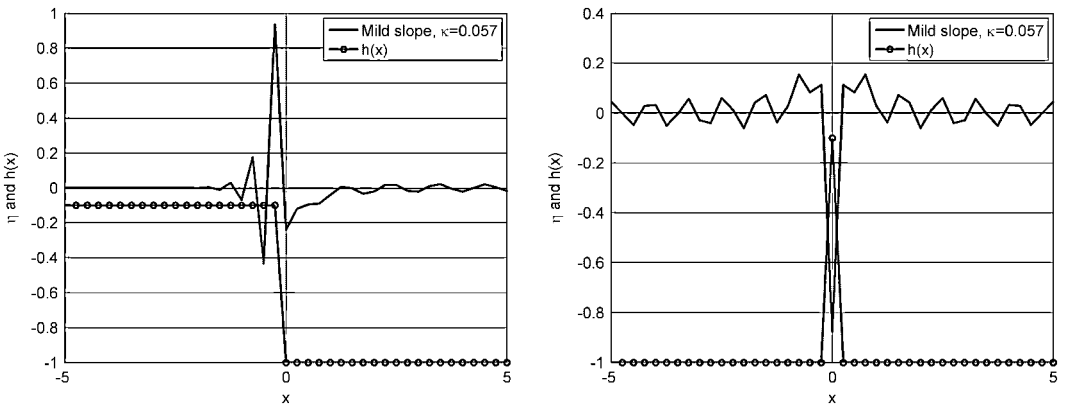

Figure A7. Unstable surface elevation waveforms for the mild-slope model with $\kappa = 0.057$ over a step-shelf (left panel) and a spike (right panel). Basin width $W = 10$, minimum depth $h_m = 0.1$, step length $L = 0.25$, spike width $L = 0.5$, and $\Delta x = 0.25$.

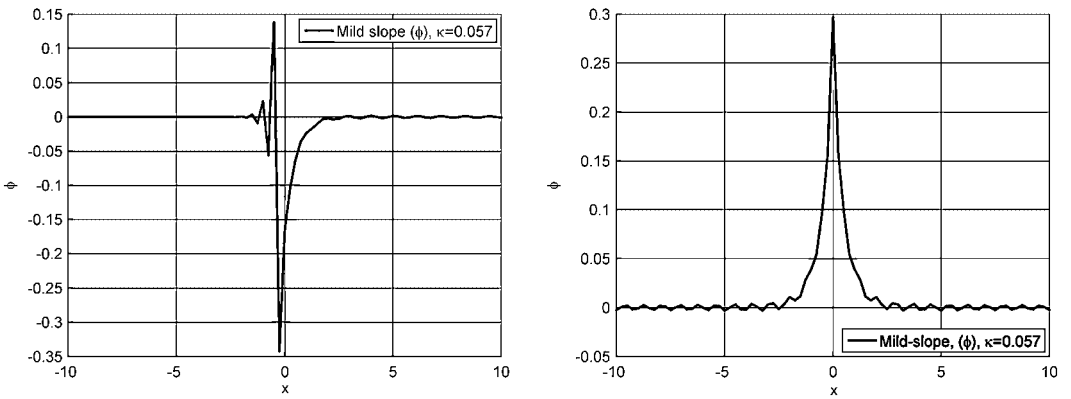

Figure A8. Unstable potential waveforms for the mild-slope model with $\kappa = 0.057$ over a step-shelf (left panel) and a spike (right panel). Basin width $W = 10$, minimum depth $h_m = 0.1$, step length $L = 0.25$, spike width $L = 0.5$, and $\Delta x = 0.25$.

- *Generalized velocity formulation with* $z_\alpha / h = -1$. The unstable modes are confined to geometries with coarse grid resolutions. Hence, when computing eigenvalues for the shelves and sea mounts shown in Figures A9–A10, no unstable modes were found.
- *Standard potential formulation.* For the smallest values of L/h_m, the modes display spatial oscillations on the grid scale, whereas for the largest values of L/h_m, smoother oscillations are evident.

A.3. Limit values for type I instabilities in infinite basins

Here we employ the procedure outlined in Section 5.2.3 to type I instabilities ($\tilde{\gamma} = 0$, $\tilde{\omega} = i\hat{\sigma}$), in infinite basins for spikes and step-shelves for the standard velocity and potential formulations. The

DOI: 10.1002/fld

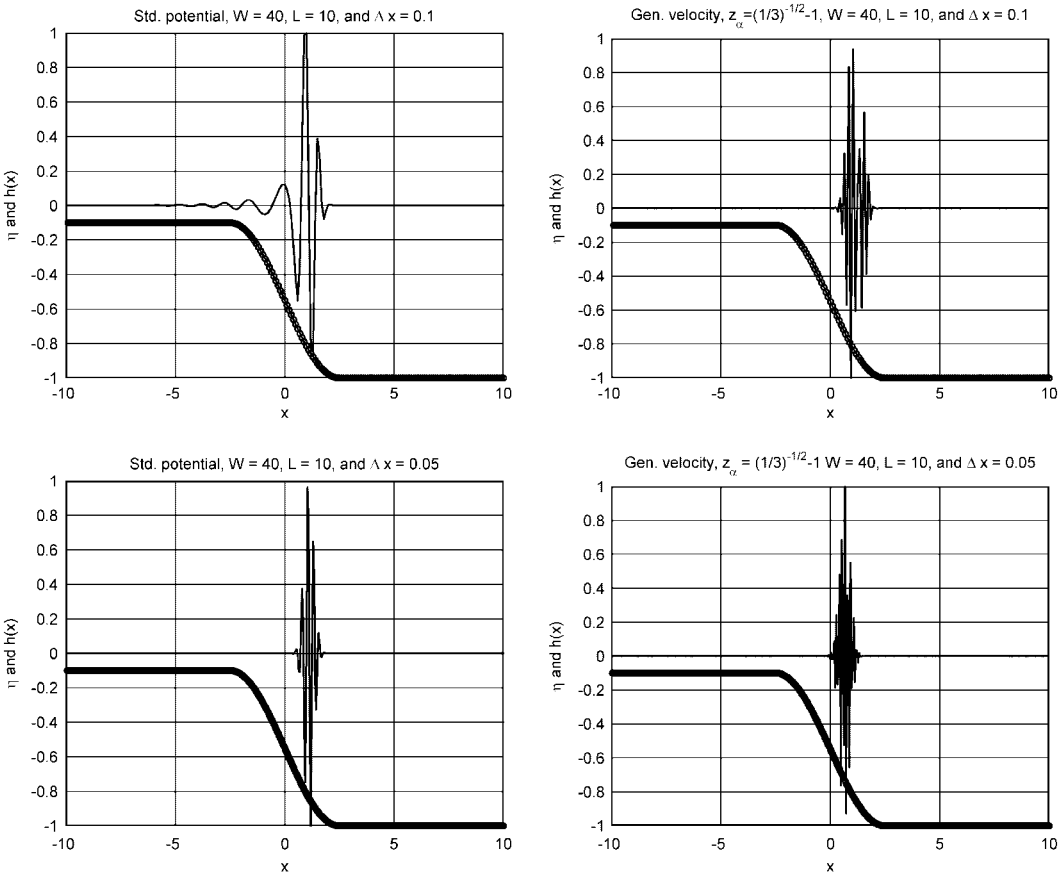

Figure A9. Unstable waveforms for shelves with minimum depths $h_{\mathrm{m}}=0.1$, using the standard potential model (left panels), and the generalized velocity model with $z_\alpha/h=\sqrt{\frac{1}{3}}-1$ (right panels). The curves with circular markers show the depth $h(x)$, while the surface elevation η is given as lines with dotted markers.

determinant of the linear equation set (node values localized to the non-constant depth region and far-field amplitudes) is denoted by f and the growth factors $\hat{\sigma}$, defined below Equation (17), are determined by

$$f(\hat{\sigma}^2, \Delta x, h_{\mathrm{m}})=0$$

which implies that roots for $\hat{\sigma}^2$ in principle are given as functions of h_{m} and Δx. The trivial solution $\hat{\sigma}=0$ corresponds to a constant surface elevation and zero velocity. The other roots for $\hat{\sigma}^2$ may change sign on particular curves in the $h_{\mathrm{m}}, \Delta x$ plane. A positive value for $\hat{\sigma}^2$ corresponds to instability, while negative values imply solutions with pure fluctuations in the far field. These solutions are nothing more than incident periodic waves that are reflected and transmitted at the

DOI: 10.1002/fld

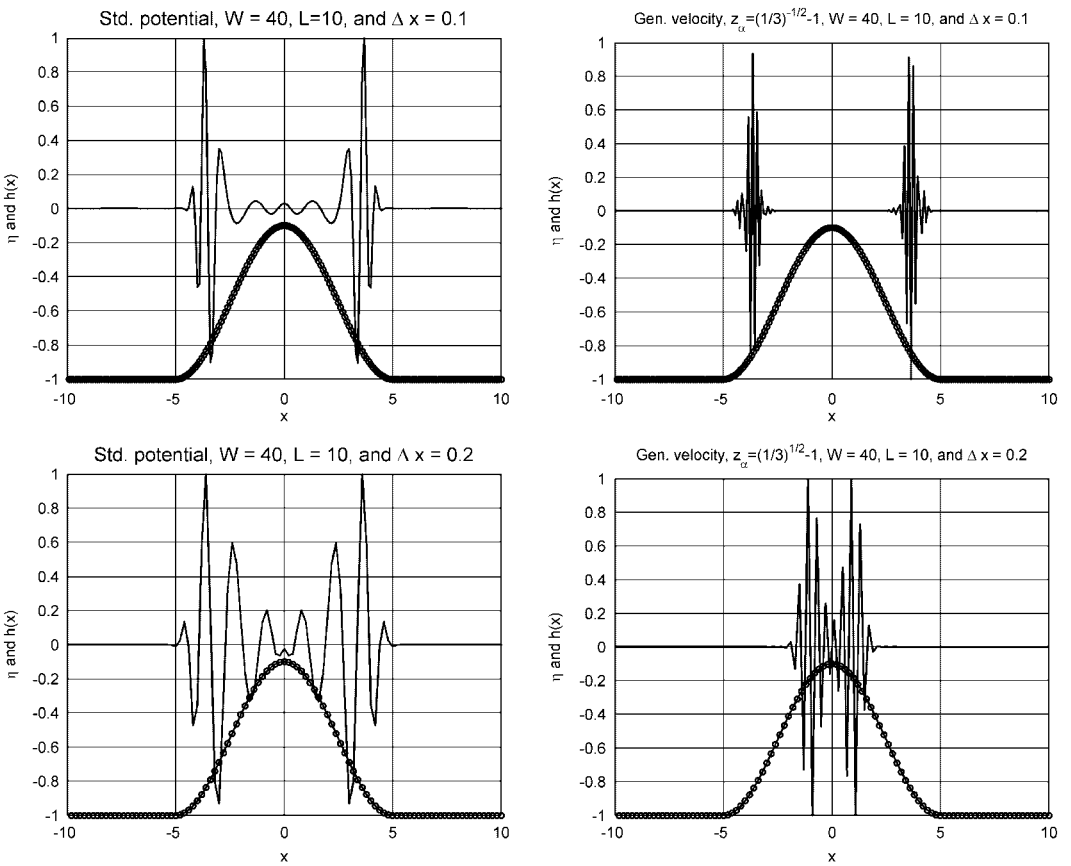

Figure A10. Unstable waveforms for sea mounts with minimum depths $h_m = 0.1$, using the standard potential model (left panels), and the generalized velocity model with $z_\alpha/h = \sqrt{\frac{1}{3}} - 1$ (right panels). The curves with circular markers show the depth $h(x)$, while the surface elevation η is given as lines with dotted markers.

bathymetric feature and described in the present formalism. Curves where $\hat{\sigma} = 0$ are thus stability limits.

A.3.1. Standard velocity model. For this model the number of unknowns in the linear set is two, both for the step-shelf and the spike, for which we assume a symmetric solution. We then arrive at the simple expressions

$$f(\hat{\sigma}^2, \Delta x, h_m) = \left(\frac{1}{\Delta x^2} + \frac{\hat{\sigma}^2}{6\Delta x^2}(3h_m - 1)\right)\left(\frac{2}{\Delta x^2} + \frac{\hat{\sigma}^2 h_m}{\Delta x^2}\left(1 - \frac{h_m}{3}\right)\right) - \left(\frac{\kappa_1 - 2}{\Delta x^2} - \hat{\sigma}^2\left(1 - \frac{\kappa_1 - 2}{3\Delta x^2}\right)\right)\left(-\frac{2}{\Delta x^2} - \hat{\sigma}^2\left(1 + \frac{2h_m^2}{3\Delta x^2}\right)\right) \quad \text{(A8)}$$

DOI: 10.1002/fld

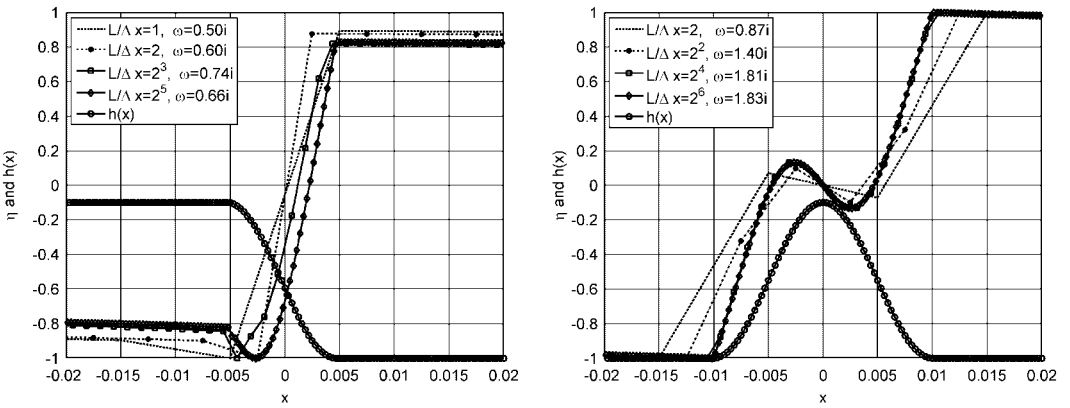

Figure A11. Surface elevations for different values of Δx for the improved velocity model. Left panel shelf with parameters $W=0.2$, $L=0.01$, right panel sea mount with parameters $W=0.2$, $L=0.02$.

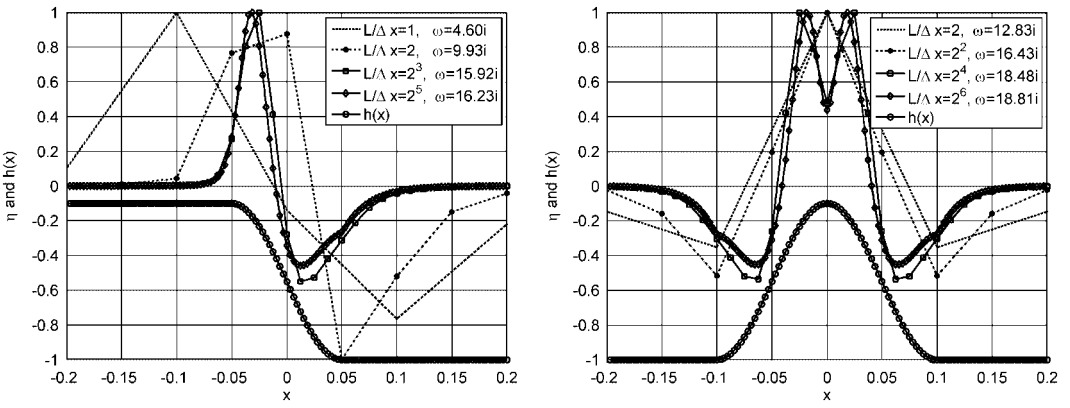

Figure A12. Surface elevations for different values of Δx for the improved potential model. Left panel shelf with parameters $W=2$, $L=0.1$, right panel sea mount with parameters $W=2$, $L=0.2$.

for the spike and

$$f(\hat{\sigma}^2,\Delta x,h_{\mathrm{m}})=\left(\frac{h_{\mathrm{m}}}{\Delta x^2}+\frac{\hat{\sigma}^2}{2\Delta x^2}\left(1-\frac{1}{3}\right)\right)\left(\frac{1}{\Delta x^2}+\frac{\hat{\sigma}^2 h_{\mathrm{m}}}{2\Delta x^2}\left(1-\frac{h_{\mathrm{m}}}{3}\right)\right)$$
$$-\left(\frac{\kappa_1-2}{\Delta x^2}-\hat{\sigma}^2\left(1-\frac{\kappa_1-2}{3\Delta x^2}\right)\right)\left(h_{\mathrm{m}}\frac{\kappa_2-2}{\Delta x^2}-\hat{\sigma}^2\left(1-\frac{h_{\mathrm{m}}^2}{3\Delta x^2}(\kappa_2-2)\right)\right) \tag{A9}$$

for the shelf. To abbreviate these expressions we have used the identities

$$\kappa_1=\mathrm{e}^{-k_I(\sigma,1)\Delta x},\quad \kappa_2=\mathrm{e}^{-k_I(\sigma,h_{\mathrm{m}})\Delta x}$$

where k_I as function of σ and h is given by (17) and (18). When we substitute for κ_1 and κ_2 in the f, the expression may be factorized in $\hat{\sigma}^2$ and a complicated factor, for which the zeros define

DOI: 10.1002/fld

the non-trivial eigenvalues. The stability limits may then be found from power series expansions of the latter factor in $\hat{\sigma}^2$. For the spike we then find

$$f=\hat{\sigma}^2\left(\frac{1}{\Delta x^2}\left(-\frac{5}{6}+\frac{3}{2}h_{\mathrm{m}}-h_{\mathrm{m}}^2\right)-6+O(\hat{\sigma}^2)\right) \tag{A10}$$

We observe that the $O(\hat{\sigma}^0)$ term in the parenthesis is always negative. Hence, $\hat{\sigma}^2$ never changes sign and no unstable modes exist. For the step-shelf we obtain

$$f=\hat{\sigma}^2\left(\frac{h_{\mathrm{m}}}{\Delta x^2}(-1+h_{\mathrm{m}}+h_{\mathrm{m}}^2-h_{\mathrm{m}}^3)-2(3+4h_{\mathrm{m}}+h_{\mathrm{m}}^2)+O(\hat{\sigma}^2)\right) \tag{A11}$$

Again there are no zero crossings in the roots and we are led to conclude that the standard velocity formulation is stable for the configurations investigated.

A.3.2. Standard potential model. The standard potential formulation yields expressions for $f(\hat{\sigma}^2,\Delta x,h_{\mathrm{m}})$ that become lengthy and are hence not given here. However, for the spike expansion in powers of $\hat{\sigma}^2$ yields

$$f=\hat{\sigma}^2\left(\frac{h_{\mathrm{m}}+1}{2\Delta x^2}\left(1-\frac{(1-h_{\mathrm{m}})^2}{3\Delta x^2}\right)+O(\hat{\sigma}^2)\right)\equiv\hat{\sigma}^2(a+O(\hat{\sigma}^2)) \tag{A12}$$

where we have defined the zeroth-order term, a,

$$a=\frac{1}{\Delta x^2}\frac{h_{\mathrm{m}}+1}{2}-\frac{1}{3\Delta x^4}\frac{h_{\mathrm{m}}+1}{2}(1-h_{\mathrm{m}})^2 \tag{A13}$$

for use in the corresponding equation for the step-shelf that reads

$$f=\hat{\sigma}^2\left(a\left\{\frac{3(1+h_{\mathrm{m}})}{2h_{\mathrm{m}}}+2+\left(\frac{1-h_{\mathrm{m}}^2}{6\Delta x^2}\right)^2\right\}+O(\hat{\sigma}^2)\right) \tag{A14}$$

The expression in the curly brackets is always positive. Thus, the stability limit is given by $a=0$ for both geometries. The stability criterion then becomes

$$\Delta x\geqslant\sqrt{\tfrac{1}{3}}(1-h_{\mathrm{m}}) \tag{A15}$$

It is emphasized that the stability criterion (A15) holds for purely imaginary ω only.

ACKNOWLEDGEMENTS

This work has been supported by the Research Council of Norway under grant 154831, by the International Centre for Geohazards (ICG), and by the Norwegian Geotechnical Institute (NGI). Moreover, the authors are thankful for the assistance of Mr S. Kvaal and Prof. H. P. Langtangen. The authors are also thankful for the constructive comments of two anonymous referees. The present article is contribution No. XX of the International Centre for Geohazards.

DOI: 10.1002/fld

REFERENCES

1. Peregrine DH. Calculation of the development of an andular bore. *Journal of Fluid Mechanics* 1966; **22**(2): 321–330.
2. Peregrine DH. Long waves on a beach. *Journal of Fluid Mechanics* 1967; **77**:417–431.
3. Madsen PA, Murray R, Sörensen OR. A new form of the Boussinesq equations with improved linear dispersion characteristics. *Coastal Engineering* 1991; **15**:371–388.
4. Nwogu O. Alternative form of Boussinesq equations for nearshore wave propagation. *Journal of the Waterways, Port, Coastal, and Ocean Engineering* 1993; **119**(6):618–638.
5. Wei G, Kirby JT, Grilli ST, Subramanya R. A fully nonlinear boussinesq model for surface waves. Part 1. Highly nonlinear unsteady waves. *Journal of Fluid Mechanics* 1995; **294**:71–92.
6. Chen Y, Liu PL-F. Modified Boussinesq equations and associated parabolic models for water wave propagation. *Journal of Fluid Mechanics* 1995; **288**:351–381.
7. Kennedy AB, Chen Q, Kirby JT, Dalrymple RA. Boussinesq modeling of wave transformation, breaking, and run-up. Part I: 1D. *Journal of the Waterways, Port, Coastal, and Ocean Engineering* 2000; **126**(1):39–47.
8. Madsen PA, Schäffer HA. A review of Boussinesq-type equations for surface gravity waves. *Advances in Coastal and Ocean Engineering*, vol. 5. World Scientific Publishing Co.: Singapore, 1999; 1–95.
9. Gobbi MF, Kirby JT, Wei G. A fully nonlinear Boussinesq model for surface waves. Part 2. Extension to $O(kh)^4$. *Journal of Fluid Mechanics* 2000; **405**:181–210.
10. Madsen PA, Bingham HB, Liu H. A new Boussinesq method for fully nonlinear waves from shallow to deep water. *Journal of Fluid Mechanics* 2002; **462**:1–30.
11. Hsiao SH, Liu PL-F, Chen Y. Nonlinear water waves propagating over a permeable bed. *Philosophical Transactions of the Royal Society of London, Series A* 2002; **458**:1291–1322.
12. Madsen PA, Bingham H, Schäffer HA. Boussinesq type formulations for fully nonlinear and extremely dispersive water waves: derivation and analysis. *Philosophical Transactions of the Royal Society of London, Series A* 2003; **459**:1004–1075.
13. Lynett PJ, Liu PL-F. A two-layer approach to wave modelling. *Proceedings of the Royal Society of London, Series A* 2004; **460**:2637–2669.
14. Madsen PA, Fuhrman DR, Wang B. A boussinesq-type method for fully nonlinear waves interacting with a rapidly varying bathymetry. *Coastal Engineering* 2006; **53**:487–504.
15. Fuhrman DR, Bingham H, Madsen PA, Thomsen PG. Linear and non-linear stability analysis for finite difference discretizations of high-order Boussinesq equations. *International Journal for Numerical Methods in Fluids* 2004; **45**:751–773.
16. Espelid TO, Berntsen J, Barthel K. Conservation of energy for schemes applied to the propagation of shallow-water inertia-gravity waves in regions with varying depth. *International Journal for Numerical Methods in Engineering* 2000; **49**:1521–1545.
17. Jørstad F. Waves generated by slides in norwegian fjords and lakes. *Insitute publication 79*, Norwegian Geotechnical Institute, 1968.
18. Harbitz CB, Pedersen G, Gjevik B. Numerical simulation of large water waves due to landslides. *Journal of Hydraulic Engineering* 1993; **119**:1325–1342.
19. Langtangen HP, Pedersen G. Computational models for weakly dispersive nonlinear water waves. *Computer Methods in Applied Mechanics and Engineering* 1998; **160**:337–358.
20. Peregrine DH. Equations for water waves and the approximation behind them. In *Waves on Beaches*, Meyer RE (ed.). Academic Press: New York, 1972; 357–412.
21. Wu TY. Long waves in ocean and coastal waters. *Proceedings of the ASCE, Journal of Engineering Mechanics Division*, vol. 107, 1981; 501–522.
22. Beji S, Nadaoka K. A formal derivation and numerical modelling of the improved Boussinesq equations for varying depth. *Ocean Engineering* 1996; **23**(8):691–704.
23. Pedersen G. Three-dimensional wave patterns generated by moving disturbances at transcritical speeds. *Journal of Fluid Mechanics* 1988; **196**:39–63.
24. Lapack Users' Guide Third Edition. URL: www.netlib.org/lapack/lug/lapack_lug.html.
25. Forsythe GE, Malcolm MA, Moler CB. *Computer Methods for Mathematical Computations*. Prentice-Hall: Englewood Cliffs, NJ, 1976.
26. Glimsdal S, Pedersen G, Atakan K, Harbitz CB, Langtangen HP, Løvholt F. Propagation of the Dec. 26, 2004 Indian Ocean Tsunami: effects of dispersion and source characteristics. *International Journal of Fluid Mechanics Research* 2006; **33**(1):15–43.

DOI: 10.1002/fld

27. Kirby JT. Funwave software download page, 1998. URL: http://chinacat.coastal.udel.edu.
28. Lynett PJ, Liu PL-F. Coulwave model page, 2004. URL: http://ceprofs.tamu.edu/plynett/COULWAVE/default.htm.
29. Woo J-K, Liu PL-F. Finite element model for modified Boussinesq equations. I: model development. *Journal of the Waterways, Port, Coastal, and Ocean Engineering* 2004; **130**(1):1–16.
30. Løvholt F, Pedersen G, Gisler G. Oceanic propagation of a potential tsunami off La Palma Island. *Journal of Geophysical Research* 2008; **113**(C09026). DOI: 10.1029/2007JC004603.